remote sensing

MDPI

Article

Retrieval of Black Carbon Absorption Aerosol Optical Depth from AERONET Observations over the World during 2000–2018

Naghmeh Dehkhoda [1], Juhyeon Sim [1], Sohee Joo [1], Sungkyun Shin [2] and Youngmin Noh [3,*]

[1] Division of Earth Environmental System Science, Pukyong National University, Busan 48513, Korea; melody87@pukyong.ac.kr (N.D.); sjh10120901@pukyong.ac.kr (J.S.); thgml1gh@pukyong.ac.kr (S.J.)
[2] Division of Climate & Environmental Research, Seoul Institute of Technology, Seoul 03909, Korea; skyun@sit.re.kr
[3] Department of Environmental Engineering, Pukyong National University, Busan 48513, Korea
* Correspondence: nym@pknu.ac.kr; Tel.: +82-51-629-6526

Abstract: Black carbon (BC) absorption aerosol optical depth ($AAOD_{BC}$) defines the contribution of BC in light absorption and is retrievable using sun/sky radiometer measurements provided by Aerosol Robotic Network (AERONET) inversion products. In this study, we utilized AERONET-retrieved depolarization ratio (DPR, δ^P), single scattering albedo (SSA, ω), and Ångström Exponent (AE, å) of version 3 level 2.0 products as indicators to estimate the contribution of BC to the absorbing fractions of AOD. We applied our methodology to the AERONET sites, including North and South America, Europe, East Asia, Africa, India, and the Middle East, during 2000–2018. The long-term $AAOD_{BC}$ showed a downward tendency over Sao Paulo (-0.001 year^{-1}), Thessaloniki (-0.0004 year^{-1}), Beijing (-0.001 year^{-1}), Seoul (-0.0015 year^{-1}), and Cape Verde (-0.0009 year^{-1}) with the highest values over the populous sites. This declining tendency in $AAOD_{BC}$ can be attributable to the successful emission control policies over these sites, particularly in Europe, America, and China. The $AAOD_{BC}$ at the Beijing, Sao Paulo, Mexico City, and the Indian sites showed a clear seasonality indicating the notable role of residential heating in BC emissions over these sites during winter. We found a higher correlation between $AAOD_{BC}$ and fine mode AOD at 440 nm at all sites except for Beijing. High pollution episodes, BC emission from different sources, and aggregation properties seem to be the main drivers of higher $AAOD_{BC}$ correlation with coarse particles over Beijing.

Keywords: aerosol optical depth (AOD); absorption aerosol optical depth (AAOD); black carbon (BC); Ångström Exponent (AE, å); single scattering albedo (SSA, ω); depolarization ratio (DPR, δ^P)

Citation: Dehkhoda, N.; Sim, J.; Joo, S.; Shin, S.; Noh, Y. Retrieval of Black Carbon Absorption Aerosol Optical Depth from AERONET Observations over the World during 2000–2018. *Remote Sens.* **2022**, *14*, 1510. https://doi.org/10.3390/rs14061510

Academic Editor: Carmine Serio

Received: 4 February 2022
Accepted: 17 March 2022
Published: 21 March 2022

1. Introduction

Natural and anthropogenic aerosols interact with solar radiation through absorption and scattering and can cause regional-to-global climate change by their direct and indirect effects on the earth-atmosphere energy balance [1]. Black carbon (BC) is one of the main light-absorbing aerosol species in the atmosphere, which plays a substantial role in global warming due to its strong absorption properties [2]. Moreover, the nucleation properties of BC change the patterns of cloud formation and microphysical properties, and accordingly, aerosol indirect radiative forcing [3]. The significant emissions of BC originate from human activities, such as heating and transportation, when fossil fuels (such as gasoline, oil, and coal), biomass, and biofuels are burnt incompletely [4]. In recent decades, BC emissions have increased drastically along with population growth, urbanization, industrialization, and economic development, BC-related research, particularly in urban and metropolitan areas, and this has attracted remarkable attention worldwide [5–7].

Remote sensing technologies such as satellites and ground-based networks play a prominent role in monitoring and characterizing aerosols and providing insight into the optical properties of atmospheric aerosols. Aerosol Robotic Network (AERONET) has provided continuous and highly accurate ground-based measurements of aerosol products,

including aerosol optical depth (AOD), single scattering albedo (SSA, ω), depolarization ratio (DPR, δ^p), and particle size distribution using CIMEL sun/sky radiometers for more than 25 years [8]. AOD is a measure of columnar aerosol loading, and it can be used to evaluate the impact of aerosols on weather and climate [9]. Further, AERONET provides absorption aerosol optical depth (AAOD), which defines the share of solar beam absorbed by the light-absorbing aerosols such as carbonaceous aerosols, black carbon, or mineral dust [10]. In dust-free conditions, BC can be considered as the primary source of light-absorbing atmospheric particles; however, the role of brown carbon (BrC) in light absorption is not negligible [11]. As aerosol plumes generally contain a vast diversity of aerosol particles, there is still significant ambiguity in separating the share of solar light absorbed by BC in the atmosphere. Despite the data availability on atmospheric aerosols and the significance of the light-absorbing ability of BC in climate change, few studies attempt to estimate the light-absorbing properties of BC on a global scale for the long term. Koven et al. [12] developed a method to separate the absorption induced by BC and dust particles using complex refractive indices and wavelength dependence of light-absorption from AERONET observations. Shin et al. [13] extended a methodology to classify dust and non-dust aerosol types and estimate the contribution of non-dust particles and BC in light absorption in a mixed aerosol plume. Sun et al. [14] compared the variations in black carbon absorption aerosol optical depth ($AAOD_{BC}$) and dust absorption aerosol optical depth ($AAOD_d$) in China for 40 years.

In this study, we utilized AERONET-retrieved DPR, ω, and Ångström Exponent (AE, å) of version 3 level 2.0 products as indicators to estimate the contributions of BC to the absorbing fractions of AOD. We applied our methodology to the AERONET sites, which are primarily located and affected by adjacent deserts and anthropogenic particles, including North and South America (Mexico City and Sao Paulo), Europe (Venice and Thessaloniki), Africa (IER-Cinzana, Ilorin, and Cape Verde), India (Kanpur and Gandhi College), Middle East (Solar Village and Mezaira), and East Asia (Beijing, Seoul, and Taipei) during the period 2000–2018. The main focus of this work was set on the determination of $AAOD_{BC}$ using aerosol optical properties and comparing its yearly, monthly, and seasonal variations during the two recent decades with the existing research on a global scale. To evaluate our $AAOD_{BC}$ retrieval methodology, we applied the methodology to the different AERONET sites for the long term. The annual and monthly $AAOD_{BC}$ values and trends are compared with other research results.

This manuscript is structured as follows: Section 2 includes a description of the materials and methods, divided into subsections dedicated to data and observation sites and methodology; Section 3 describes the results and statistical analysis; discussion is presented in Section 4; and finally, our work is summarized in Section 5, and the findings are concluded.

2. Materials and Methods

2.1. AERONET Data and Study Area

AERONET (http://aeronet.gsfc.nasa.gov/ accessed on 15 March 2021), known as the global sun/sky radiometer network, provides consistent and ground-truth measurements of aerosol optical, microphysical, and radiative properties [8]. As of 2018, the number of AERONET observation sites has increased to more than 600 sites worldwide. AERONET inversion code enables data accessibility on aerosol optical properties in the total atmospheric column by the sun/sky radiometers. The AERONET version 3 algorithm is based on the version 2 algorithm with various updates, which offer entirely automatic cloud screening and instrument quality control. The version 3 aerosol datasets are computed at three data quality levels, level 1.0: unscreened, level 1.5: cloud-screened, and Level 2.0: quality-assured. The aerosol level 2.0 cloud-screened and quality-assured datasets are downloadable after post-field calibration. AERONET version 3 level 2.0 inversion products provide DPR, AOD, ω, and other aerosol properties at several wavelengths, including 440, 675, 870, and 1020 nm. Further, inversion product outputs process the potential errors (both random and systematic) for most of the retrieved characteristics. The AERONET-retrieved

AOD uncertainty is estimated as 0.01 to 0.02 depending on the wavelength in a clear sky and cloud contamination-free condition [13]. Moreover, the uncertainties arising from ω, an important parameter controlling aerosol direct radiative forcing, were estimated to be of the order of 0.03 [15]. The calibrated sky radiance measurements typically have uncertainties lower than 5%. AERONET level 2.0 product includes inversion results for observations with AODs larger than 0.4 at 440 nm. Chew et al. [16] estimated up to 0.03 of AOD bias in AERONET version 3 level 2.0 measurements owing to the prevalence of cirrus clouds in Singapore.

To investigate the $AAOD_{BC}$ variations on a global scale during the long term, we selected the AERONET sites according to the following characterizations:

1. The AERONET observation data should be available for almost half of the study period at each site (more than nine years), allowing us to assess the long-term $AAOD_{BC}$ variations.
2. Each AERONET observation site should contain at least ten observations annually in different months (the years with lower observations were excluded from this study).
3. The chosen sites must represent variations in aerosol optical characteristics due to mixing dust particles and anthropogenic aerosols during long-range transportation.

Accordingly, we selected 14 AERONET sites consistent with our considerations, allowing us to apply our methodology in different locations worldwide. The selected AERONET sites and their geolocation information are listed in Table 1.

Table 1. The geolocation information of the selected AERONET sites.

Location	Site Geolocation Information
America	Sao Paulo (23.561°S, 46.735°W) Mexico City (19.334°N, 99.182°W)
Europe	Thessaloniki (40.630°N, 22.960°E) Venice (45.314°N, 12.508°E)
East Asia	Beijing (39.977°N, 116.381°E) Seoul_SNU (37.458°N, 126.951°E) Taipei (25.015°N, 121.538°E)
Africa	IER_Cinzana (13.278°N, 5.934°W) Ilorin (8.484°N, 4.675°E) Cape Verde (16.733°N, 22.935°W)
Middle East	Solar Village (24.907°N, 46.397°E) Mezaira (23.105°N, 53.755°E)
India	Kanpur (26.513°N, 80.232°E) Gandhi College (25.871°N, 84.128°E)

Figure 1 shows the locations of the selected AERONET sites. Open forest fires, residential carbon-containing fuels, biomass-burning, industrial sections, and transportation are the noted sources of BC globally, particularly in developing countries. Hence, the selected observation sites were considered to represent the global variations of $AAOD_{BC}$ in both developed and developing countries in the long term. In addition, most of the selected sites are located adjacent to the deserts or are affected by desert dust due to the long-range transport.

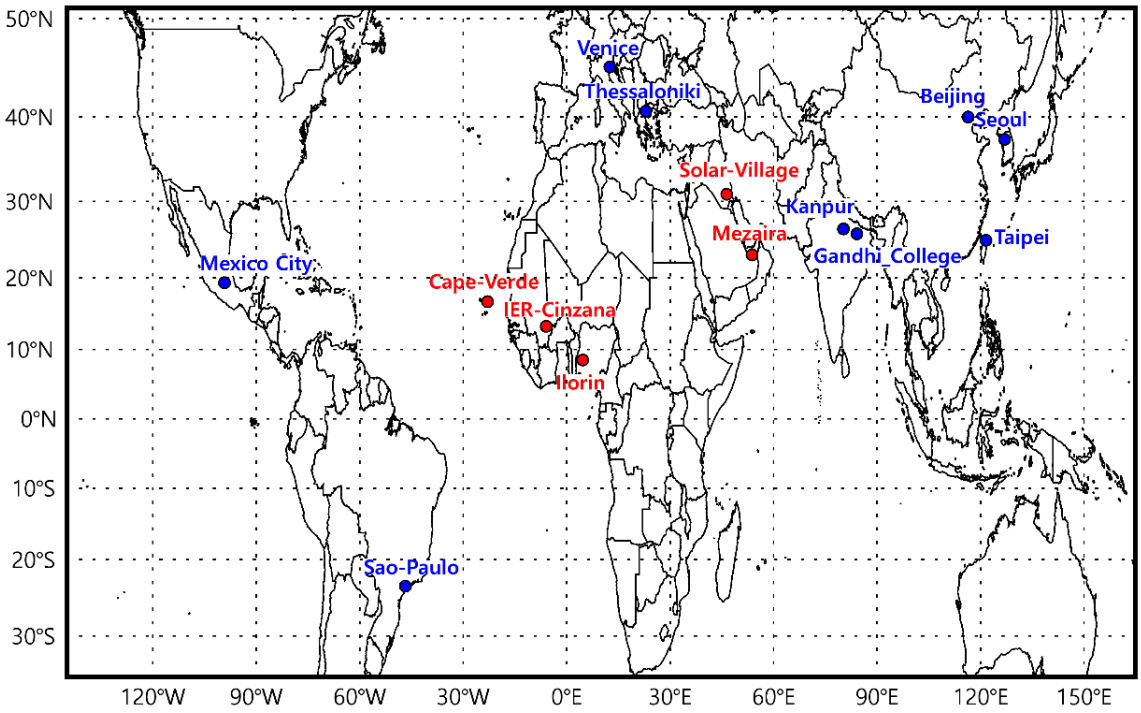

Figure 1. Locations of the selected AERONET sites (red color represents the sites with dust-dominant AAOD and blue color represents the sites with non-dust-dominant AAOD).

2.2. $AAOD_{BC}$ Calculation Methodology

Since BC is not the only light-absorber in the atmosphere, the evaluation of BC's contribution to light absorption is one of the largest uncertainty sources in assessing the earth's radiation budget [17]. Solar radiation absorption in urban and biomass-burning areas is attributed mainly to carbonaceous aerosols, largely BC. However, organic carbon (OC) has also been identified as the light absorber at visible to UV wavelengths, and the absorbing organics are referred to as BrC. Other absorbing species such as dust can contribute significantly to light absorption (dust absorbs light in short visible and UV spectrum), specifically in arid and semi-arid regions. Therefore, separating the fraction of the light absorbed by BC is still ambiguous [18]. Estimating the portion of light absorbed by BC is not complicated, provided that the fraction of light absorbed by dust particles is excluded. Previous researchers separated the dust and non-dust (pollution) species using the DPR values measured by LIDAR [19,20]. Noh et al. [21] found a high correlation coefficient between the DPR measured by LIDAR at 532 nm and retrieved from AERONET data at 1020 nm. Hence, we applied the method of Shin et al. [13] to separate dust and non-dust particles using AERONET-retrieved DPR at 1020 nm and subsequently calculated $AAOD_{BC}$ by excluding the share of light absorbed by BrC from the non-dust AAOD ($AAOD_{nd}$). This methodology was previously validated by comparing the AERONET-derived values to the ones provided by Copernicus Atmosphere Monitoring System (CAMS) aerosol reanalysis data. The authors suggested this methodology is specifically valuable at locations that show the occurrence of complex mixtures of mineral dust and anthropogenic pollution, e.g., East Asia or Southern Europe, and individual polluted cities downwind from deserts. Hence, we applied this methodology to the AERONET sites located in East Asia, Southern Europe, the Middle East, Africa, and highly polluted cities affected by the adjacent and/or transported desert dust such as the Indian and American sites.

In the following few paragraphs, we describe the removal of $AAOD_{BC}$ from the total AAOD.

Depolarization ratio (DPR, δ^p) is the ratio of the perpendicular polarization component to the parallel component of aerosol scattering [22,23]. This parameter provides more profound knowledge on particle optical and microphysical properties and can be found in

four wavelengths of 440, 675, 870, and 1020 nm from AERONET version 3 level 2.0 product measurements. Shin et al. [24] reported that distinct values of AERONET-derived DPRs at 1020 nm (δ^{p}_{1020}) can represent dust particles generated in various deserts. Dust particles originating from the Gobi desert can be represented by the δ^{p}_{1020} of 0.30 ± 0.04 and the δ^{p}_{1020} values of 0.28 ± 0.03, 0.31 ± 0.03, and 0.28 ± 0.02 represent the dust particles that originated from the Arabian, Saharan, and Great Basin deserts, respectively. δ^{p}_{1020} values greater than 0.30 indicate pure Asian dust particles, whereas values below 0.02 represent anthropogenic pollution particles. Hence, δ^{p} can be used as a distinguishing parameter to identify the contribution of dust and non-dust particles in a mixed aerosol plume. Shimizu et al. [19] separated the contribution of dust (R_d) to the total backscattering coefficient from the following equation assuming the spherical and non-spherical particles are externally mixed:

$$R_d = \frac{\left(1+\delta^{p}_{d}\right)\left(\delta^{p}_{1020}-\delta^{p}_{nd}\right)}{\left(1+\delta^{p}_{1020}\right)\left(\delta^{p}_{d}-\delta^{p}_{nd}\right)} \quad (1)$$

where δ^{p}_{nd} and δ^{p}_{d} indicate the δ^{p} of non-dust and dust particles at 1020 nm, respectively.

Calculation of R_d permits the derivation of dust AOD (AOD_D) from the total AOD (AOD_T) and segregation of AOD_T to non-dust AOD (AOD_{nd}) and AOD_D at 1020 nm as follows:

$$AOD_D = R_d \times AOD_T \quad (2)$$

Ångström Exponent of pure desert dust ($å_D$) can be used to convert AOD_D at 1020 nm to corresponding values for other wavelengths depending on the dust origination. Previous researchers suggested the $å_D$ of 0.06 ± 0.21 and 0.14 ± 0.07 for pure Saharan and Asian dust, respectively [20,25]. Other researchers used the $å_D$ of 0.18 ± 0.10 and 0.08 ± 0.07 for the Arabian and Great Basin Desert dust [24]. Consequently, AOD_D at other wavelengths can be derived as

$$AOD_{D,\lambda} = AOD_{D,1020} \times \left(\frac{1020\ nm}{\lambda}\right)^{å_D} \quad (3)$$

here, λ and subscript numbers indicate the wavelengths and wavelengths in 1020 nm, respectively. The contribution of non-dust particles to the AOD_T can now be obtained as

$$AOD_{nd,\lambda} = AOD_{T,\lambda} - AOD_{D,\lambda} \quad (4)$$

Spectral dependence of aerosol ω (the fraction of intercepted light that is scattered rather than absorbed) has been used to infer the composition of the aerosol mixture. For aerosol mixtures dominated by dust absorption, the ω monotonically increases with wavelength, while that dominated by BC absorption has monotonically decreasing ω spectra [26]. Moreover, the derivation of the ω or the spectral difference of ω may provide further information on the aerosol type. For example, dust particles exhibit strong light absorption at the visible range (e.g., 440 nm) and lower light absorption at higher wavelengths. As BC particles exhibit the most robust light absorption properties at near-infrared wavelengths, the total ω (ω_T) can be split into components for dust (ω_D) and non-dust (ω_{nd}) as follows:

$$\omega_{T,\lambda} = \frac{AOD_{D,\lambda}}{AOD_{T,\lambda}}\omega_{D,\lambda} + \frac{AOD_{nd,\lambda}}{AOD_{T,\lambda}}\omega_{nd,\lambda} \quad (5)$$

By rearranging Equation (5) the ω related to non-dust particles ($\omega_{nd,\lambda}$) can be found:

$$\omega_{nd,\lambda} = \left(\omega_{T,\lambda} - \frac{AOD_{D,\lambda}}{AOD_{T,\lambda}}\omega_{D,\lambda}\right) \times \frac{AOD_{T,\lambda}}{AOD_{nd,\lambda}} \quad (6)$$

Noh et al. [21] calculated the spectral ω as 0.94, 0.98, 0.98, and 0.98 at 440, 675, 870, and 1020 nm, respectively, using data for a source region of Asian dust; Dunhuang located

in Western China (40.49° N, 94.95° E). In this study, the ω values for Arabian, Saharan, and Great Basin pure desert dust have been derived according to Shin et al. [24].

From the ω_{nd} the contribution of non-dust particles to light-absorption, the non-dust AAOD ($AAOD_{nd}$) can be computed as

$$AAOD_{nd,\lambda} = (1 - \omega_{nd,\lambda})\, AOD_{nd,\lambda} \quad (7)$$

To arrive at the contribution of BC in light absorption, the share of BrC in absorption should be excluded. As the BrC ω (ω_{BrC}) is not equal to 0., to estimate the AAOD induced by BrC ($AAOD_{BrC}$), the ω_{BrC} was included in the following equation:

$$AAOD_{BrC,\lambda} = AOD_{nd,\lambda} \times (1 - \omega_{nd,\lambda}) \times (1 - \omega_{BrC,\lambda}) \quad (8)$$

Although BC is strongly light-absorbing and a broad range of values from 0.07 to 0.3 has been reported for fresh ω_{BC}, the light absorption induced by BrC is lower than BC, and the ω_{BrC} varies between 0.77 and 0.85 [27]. We used the values of 0.77, 0.80, and 1.00 at 440, 675, and 870 nm for ω_{BrC}, respectively [28].

BC and dust particles are two fundamental light-absorbing particles in the atmosphere. Therefore, we assume that in a dust-free condition, if the share of the light absorbed by BrC is excluded, the light absorption mainly owes to BC:

$$AAOD_{BC,\lambda} = AAOD_{nd,\lambda} - AAOD_{BrC,\lambda} \quad (9)$$

In the next step after removal of $AAOD_{BC}$, we aimed to estimate whether BC particle belongs to fine or coarse mode particle categories; therefore, the calculated $AAOD_{BC}$ was compared to the values of total coarse- and fine mode AOD at 440 nm. The correlation between $AAOD_{BC}$ and coarse- or fine mode particles is discussed in the result section.

2.3. Trend Analysis Description

To plot the variations in AOD_T and $AAOD_{BC}$, we applied the linear regression to the time series data; however, trend detection in time series is complicated, specifically when parameters are not normally distributed. Since none of the analyzed aerosol parameters here are normally distributed, we, therefore, applied the non-parametric Mann−Kendall test associated with Sen's slope to detect any significant trend and estimate their magnitude using R software version 4.0.3. The description of the methods is provided below in detail.

2.3.1. Mann−Kendall Test

The Mann−Kendall (MK) test is a statistical test widely used for the trend analysis of the climatology and meteorological time series [29–31]. MK test is a non-parametric test and only requires the data to be independent, not normally distributed. As the Mk test can be applied regardless of missing data, statistical distribution, and presence of negatives in the data set, it is defined as a suitable test to apply for optical properties [32]. In this study, to better interpretation of the $AAOD_{BC}$ trends, we used two non-parametric trend analysis tests of Mann−Kendall and Sen's slope estimator.

The null hypothesis (H_0) in the MK test describes no trend in the time series against the alternative hypothesis (H_1), which states a trend in data. For the time series $x_1, \ldots, x_n$, the MK test defines the following statistic S [33,34]:

$$S = \Sigma_{i=1}^{n-1} \Sigma_{j=i+1}^{n} \operatorname{sgn}(x_j - x_i) \quad (10)$$

here n indicates the number of data points, x_i and x_j represent the data values in time series i and j (j > i), and sgn ($x_j - x_i$) is the sign function as:

$$\operatorname{sgn}(x_j - x_i) = \begin{cases} \text{if } xj - xi > 0, +1 \\ \text{if } xj - xi = 0,\ 0 \\ \text{if } xj - xi < 0, -1 \end{cases} \quad (11)$$

The variance statistic of S is given by

$$\text{Var}\ (S) = \frac{1}{18}\ [n(n-1)(2n+5) - \Sigma_{i=1}^{m}\ t_i\ (t_i-1)(2\ t_i+5) \quad (12)$$

where m describes the number of tied groups and t_i is the number of data values in the ith group. Accordingly, the standard normal test statistic Z_s (Mann−Kendall coefficient) is calculated using Equation (12):

$$Z_s = \begin{cases} \frac{S-1}{\sqrt{\text{Var}(S)}}, \text{ if } S > 0 \\ 0, \text{ if } S = 0 \\ \frac{S+1}{\sqrt{\text{Var}(S)}}, \text{ if } S < 0 \end{cases} \quad (13)$$

The positive values of Z_s show upward trends, while the negative values of Z_s indicate downward trends. The test is performed at the specific α significant level when $|Zs| > Z_{1-\alpha/2}$ the alternative hypothesis is accepted, and there is a significant trend in the time series. $Z_{1-\alpha/2}$ can be found from the standard normal distribution table. At the 5% significance level (α = 0.05), the null hypothesis (no trend) is rejected if $|Zs| > 1.96$ and rejected if $|Zs| > 2.576$ at the 1% significance level (α = 0.01). Moreover, at the 10% significance level (α = 0.1), the null hypothesis is rejected if $|Zs| > 1.645$ [35]. In the present analysis, α is considered as a 5% significance level or 95% confidence level.

2.3.2. Sen's Slope Estimator

The actual slope of trend in the sample of N pairs of data can be estimated by a non-parametric procedure developed by Sen [36]:

$$Q_i = \frac{xj\ -\ xk}{j-k} \text{ for } i = 1, \ldots, N \quad (14)$$

here x_j and x_k indicate data values at times j and k (j > k), respectively.

In the case of multiple observations in one or more time series, then $N < \frac{n(n-1)}{2}$, where n denotes the total number of observations. The median of the slope or Sen's slope estimator can be calculated as

$$Q_{med} = \begin{cases} Q_{[(N+1)/2]}\ , \text{ if N is odd} \\ \frac{Q_{[N/2]}\ +\ Q_{[(N+2)/2]}}{2}, \text{ if N is even} \end{cases} \quad (15)$$

The Q_{med} value represents the steepness of the trend, while its sign defines data trend reflection (i.e., downward or upward). Sen's method is closely linked to the MK test and has been extensively used in meteorological and AOD-related studies [37–39].

2.4. Uncertainties in $AAOD_{BC}$ Retrieval Methodology

To estimate the uncertainties in $AAOD_{BC}$ retrieval for this methodology, we calculated the Confidence Interval (CI) of $AAOD_{BC}$ at each site from 2000 to 2018. The CI measures the degree of uncertainty or the possible range around the estimate. The CI defines how stable the estimate is based on the standard errors and can be calculated as

$$\text{CI}:\ X^{-} \pm Z\ \frac{S}{\sqrt{n}} \quad (16)$$

here X^{-}, Z, and S indicate the mean values, confidence level value (here 95% is considered), and standard deviations, respectively. The number of data points is presented by n [40].

3. Results

In this section, we focus on presenting the annual variations of AOD_T, annual and monthly variations in $AAOD_{BC}$, BC ratio ($AAOD_{BC}/AOD_T$ ratio), $AAOD_{BC}/AAOD_{Total}$

ratio, and finally, the possible correlation between $AAOD_{BC}$ and fine-or coarse mode particles. Furthermore, the magnitudes and significance of the trends at each AERONET site are presented in detail. The fourteen AERONET observation sites and the number of total observations considered in this study are listed in Table 2.

Table 2. The number of the considered AERONET observation for fourteen selected sites over the period 2000–2018.

Number of AERONET Observations		
Location	**Stations**	**Total**
North & South America	**Sao Paulo**	201
	Mexico City	341
Europe	**Thessaloniki**	494
	Venice	555
East Asia	**Beijing**	1313
	Taipei	361
	Seoul	822
Africa	**Cape Verde**	720
	IER-Cinzana	1207
	Ilorin	998
Middle East	**Mezaira**	699
	Solar Village	1262
India	**Gandhi College**	821
	Kanpur	2379

Before presenting the results, we clarify that through the rest of this paper, the term "significant" or ''significance" refers to "statistically significant at the 95% confidence level or interval" based on the MK and Sen's slope test results. Table 3 lists the significance and magnitude of the trends from the MK and Sen's slope test at all the AERONET sites included in this study.

3.1. Variations of Annual Mean AOD_T and $AAOD_{BC}$

Figure 2 indicates the variations of the annual mean AOD_T at 440 nm for each site from 2000 to 2018. Based on the MK test results, the AOD_T trend is significant over the European sites, Mexico City, and Beijing, indicating a decreasing tendency. In comparison, Kanpur showed a significant positive trend in AOD_T. Sao Paulo showed roughly higher values of AOD_T compared to the Mexico City site. Both European sites (i.e., Thessaloniki and Venice) represented a significant downward tendency and comparable values in AOD_T (between 0.3 and 0.75). Although the AOD_T fluctuations vary in different sites, the American and European sites represented nearly similar variations (between 0.3 and 0.9) during the two past decades. In the case of East Asian sites, Beijing denoting the highest AOD_T, higher than 0.9, demonstrated a significant downward trend (-0.011 year^{-1}) from 2000 to 2018. The lack of measurements from 2003 to 2011 restricted observing a consistent trend over Seoul; however, lower values were observed in Seoul compared to Beijing. The Taipei site showed the lowest AOD_T (less than 0.8) in comparison to the other East Asian sites.

Table 3. Location, sites, number of observations used in the analysis (N), the Mann−Kendall z and p values, and Sen's slope for AOD_T, $AAOD_{BC}$, BC Ratio ($AAOD_{BC}/AOD_T$), and $AAOD_{BC}/AAOD_T$ ratio at 440 nm at the 14 selected AERONET sites. Bold values indicate trends at a 95% significance level and their magnitude.

Location	Site	N	AOD_T (440 nm)			N	$AAOD_{BC}$ (440 nm)			N	BC Ratio ($AAOD_{BC}/AOD_T$)			N	$AAOD_{BC}$ to $AAOD_{Total}$ $AAOD_{BC}/AAOD_T$ Ratio		
			Mann−Kendall		Sen's Slope		Mann−Kendall		Sen's Slope		Mann−Kendall		Sen's Slope		Mann−Kendall		Sen's Slope
			z Value	p-Value			z Value	p-Value			z Value	p-Value			z Value	p-Value	
Americas	Sao Paulo	11	−0.155	0.876	−0.005	11	−1.98	0.051	**−0.001**	11	0	1	0.00	11	−1.245	0.212	−0.006
	Mexico City	14	−3.065	0.0021	**−0.01**	14	−1.423	0.154	−0.0005	14	−0.12	0.5	−0.0001	14	−0.32	0.74	0.00
Europe	Thessaloniki	13	−2.867	0.004	**−0.006**	13	−2.013	0.044	**−0.0004**	13	−1.98	0.012	**−0.001**	13	**−1.98**	**0.046**	**−0.015**
	Venice	18	−3.030	0.002	**−0.009**	18	−0.227	0.820	0.000	18	0.530	0.59	+0.0001	18	**−2.42**	**0.015**	**−0.006**
East Asia	Beijing	17	−2.43	0.015	**−0.011**	16	−1.98	0.0139	**−0.001**	16	0.045	0.096	0.00	16	**−1.98**	**0.05**	**−0.006**
	Seoul	9	−1.46	0.25	−0.004	9	−3.023	0.002	**−0.0015**	9	−1.98	0.04	**−0.0011**	9	**−1.196**	**0.05**	**−0.018**
	Taipei	15	−0.94	0.34	−0.005	15	−1.088	0.276	−0.0005	15	−0.989	0.322	−0.0008	15	**−3.16**	**0.0015**	**−0.0094**
Africa	Cape Verde	16	−0.151	0.87	−0.0004	15	−2.672	0.007	**−0.0009**	16	−3.10	0.0018	**−0.0014**	16	**−3.06**	**0.002**	**−0.0019**
	IER-Cinzana	14	−0.328	0.74	−0.001	14	−0.65	0.51	−0.0001	14	0.52	0.58	+0.0001	14	0.00	1	0.00
	Ilorin	15	−0.296	0.766	−0.005	15	0.98	0.32	+0.001	15	1.187	0.23	+0.0011	15	0.98	0.32	+0.003
Middle East	Mezaira	11	0.618	0.537	+0.0044	11	−0.622	0.533	−0.0002	11	0.10	0.53	0.00	11	−0.34	0.73	−0.0008
	Solar Village	13	1.89	0.058	+0.010	12	1.57	0.11	+0.001	12	1.44	0.014	+0.0012	12	1.028	0.303	+0.0012
India	Gandhi College	10	0.178	0.758	+0.007	10	0.17	0.85	+0.0004	10	−0.17	0.85	−0.0004	10	1.25	0.21	+0.02
	Kanpur	18	2.045	0.040	**+0.009**	17	−1.287	0.197	−0.0005	17	−2.677	0.007	**−0.0011**	17	0.86	0.38	+0.0031

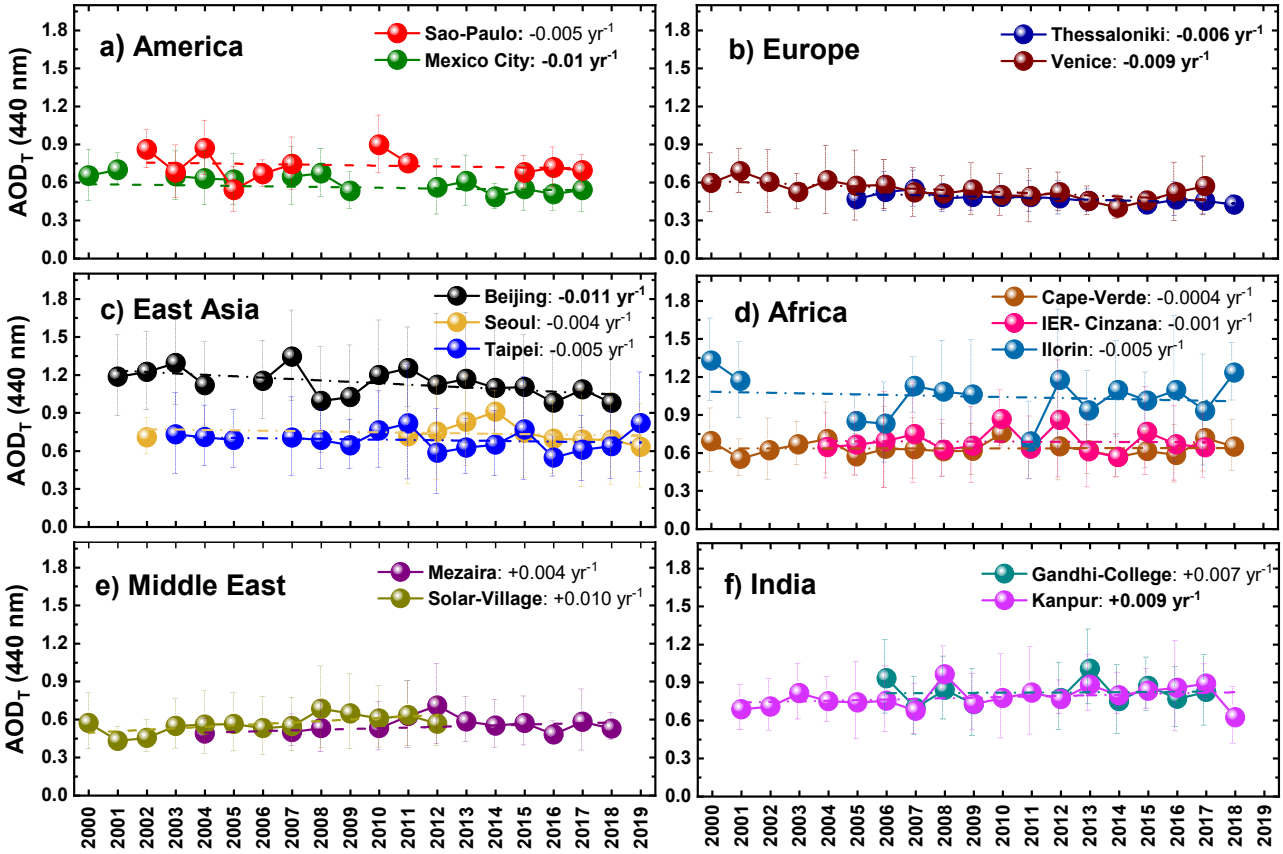

Figure 2. Variations of annual mean AOD_T at 440 nm from 2000 to 2018 at fourteen sites. Error bars represent the standard deviation of the annual averages. (units AOD_T $year^{-1}$).

None of the African and the Middle Eastern sites indicated a significant trend in AOD_T during 2000–2018. The AOD_T showed higher values at the Ilorin site (between 0.7 and 1.35) compared to the other African and Middle Eastern sites with the AOD_T variations between 0.3 to 0.9. Like the Middle Eastern sites, the AOD_T represented comparable values over Gandhi College and Kanpur. The majority of the sites with significant trends depicted negative trends in AOD_T, except for the Kanpur site, which exhibited a considerably positive trend with Sen's slope of +0.009. The largest significant decline was found over Beijing, reaching −0.011. Overall, the maximum AOD_T values were identified over Beijing and Ilorin with variations higher than 0.7 throughout 2000–2018.

The $AAOD_{BC}$ trends for the fourteen AERONET sites during the study period are presented in Figure 3. According to the statistical tests, the $AAOD_{BC}$ trends over Sao Paulo, Thessaloniki, Beijing, Seoul, and Cape Verde significantly declined from 2000 to 2018. The top significant falling trend was identified over Seoul (-0.0015 $year^{-1}$), while the Cape Verde with the Sen's slope of −0.0009 demonstrated the minimum significant declining tendency. Though both the Indian sites represented exceptional values of $AAOD_{BC}$ (higher than 0.03) compared to Mezaira and Solar Village (lower than 0.03), we could not approve any significant trend in annual mean $AAOD_{BC}$ neither over Middle Eastern nor the Indian sites.

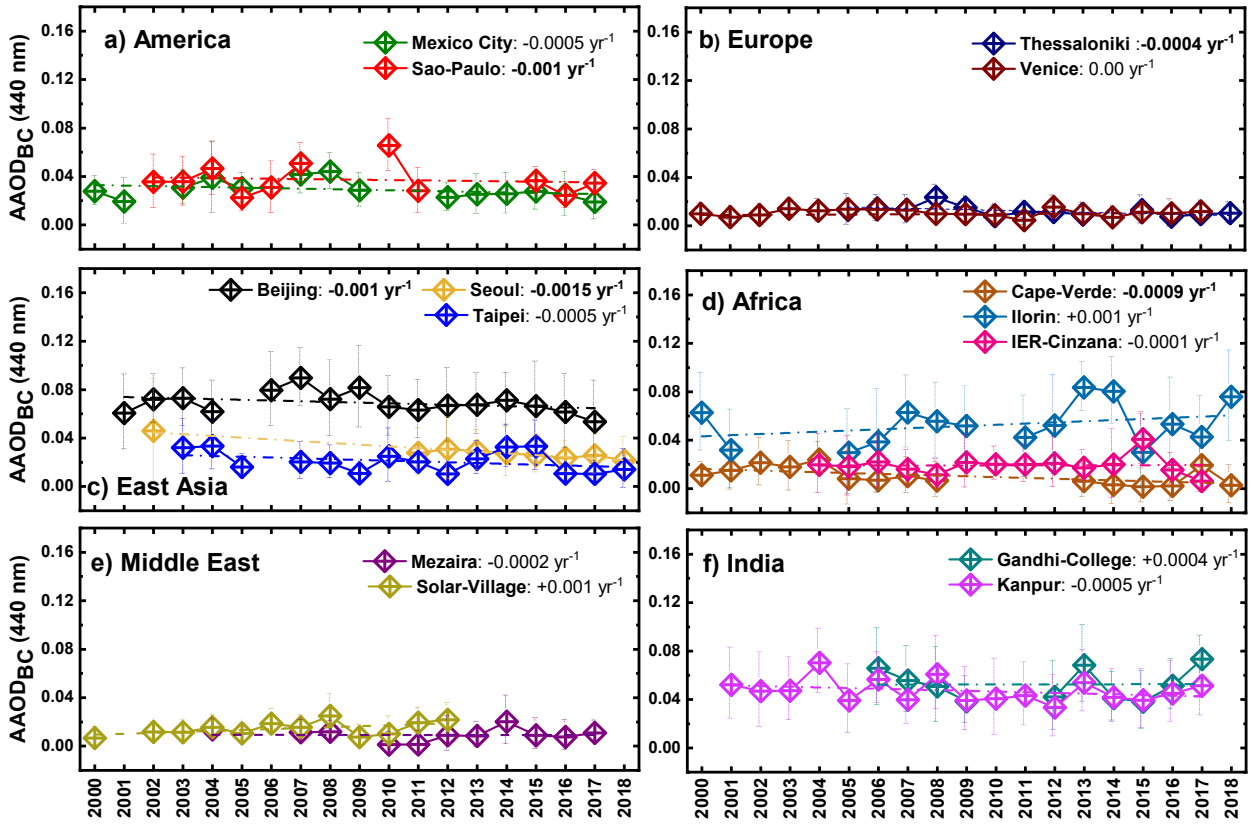

Figure 3. Variations of annual mean $AAOD_{BC}$ at 440 nm from 2000 to 2018 at fourteen sites. Error bars represent the standard deviation of the annual averages. (units $AAOD_{BC}$ year^{-1}).

For the East Asian sites, both Beijing and Seoul showed negative $AAOD_{BC}$ trends with the magnitude of -0.001 and -0.0015 year^{-1}, respectively. Although we could not detect any significant $AAOD_{BC}$ trend over Taipei; however, lower values of $AAOD_{BC}$ (less than 0.04) were observed in this site compared to Beijing and Seoul. With the highest $AAOD_{BC}$ (picked at approximately 0.09 at some years, nearly ten times higher than the European and Middle Eastern sites), Beijing and Ilorin exhibited higher values during the past 18 years. Sao Paulo indicated higher $AAOD_{BC}$ than the Mexico City site in some years; also, we detected higher $AAOD_{BC}$ in Ilorin compared to Cape Verde and IER_Cinzana. A significant downward tendency (-0.001 year^{-1}) was found over Sao Paulo. The European and Middle Eastern sites with $AAOD_{BC}$ less than 0.04 demonstrated the lowest and almost identical variations in $AAOD_{BC}$ throughout the study period. Thessaloniki, with the $AAOD_{BC}$ trend magnitude of -0.0004, demonstrated a significant decreasing trend. No remarkable trend was observed over the Indian sites, while higher $AAOD_{BC}$ was found in both sites compared to the European and Middle Eastern sites.

We also estimated the variations of the monthly mean $AAOD_{BC}$ at 440 nm over the study area from 2000 to 2018; the results are presented in Figure 4. The $AAOD_{BC}$ at Beijing, Sao Paulo, Mexico City, and the Indian sites represented a common monthly variation, enhanced in $AAOD_{BC}$ over the cold months. $AAOD_{BC}$ over Beijing was the highest, peaked from October to March and again in July, all year round. The $AAOD_{BC}$ at Thessaloniki and Venice is slightly higher during December-January than other months. The highest monthly $AAOD_{BC}$ appeared in January and February over Seoul and in March at Taipei, respectively. The Mexico City and Sao Paulo sites showed the high values of $AAOD_{BC}$ in the wintertime. For Ilorin, $AAOD_{BC}$ exhibits relatively moderate values (less than 0.04) during March–August, decreasing drastically from August to October and then steadily reaching up to ~0.08 during December–February. The $AAOD_{BC}$ over Cape Verde and IER-Cinzana are much higher in December-January than those found in other months of

the year. The monthly mean $AAOD_{BC}$ values vary threefold at the Indian sites, ranging from 0.02–0.03 during June–September to 0.06–0.07 during November–December. Further, enhanced $AAOD_{BC}$ was found from April to May at both sites; Gandhi College and Kanpur. We detected a comparatively higher variability in $AAOD_{BC}$ from December to January and August in Mezaira and Solar-Village (elevated values remained steady until October at the Solar-Village site). Although $AAOD_{BC}$ represents a distinct monthly variation in some sites such as the Americas, Beijing, Ilorin, and the Indian sites, the monthly $AAOD_{BC}$ changes in the other sites do not vary a lot and are not clearly distinguishable.

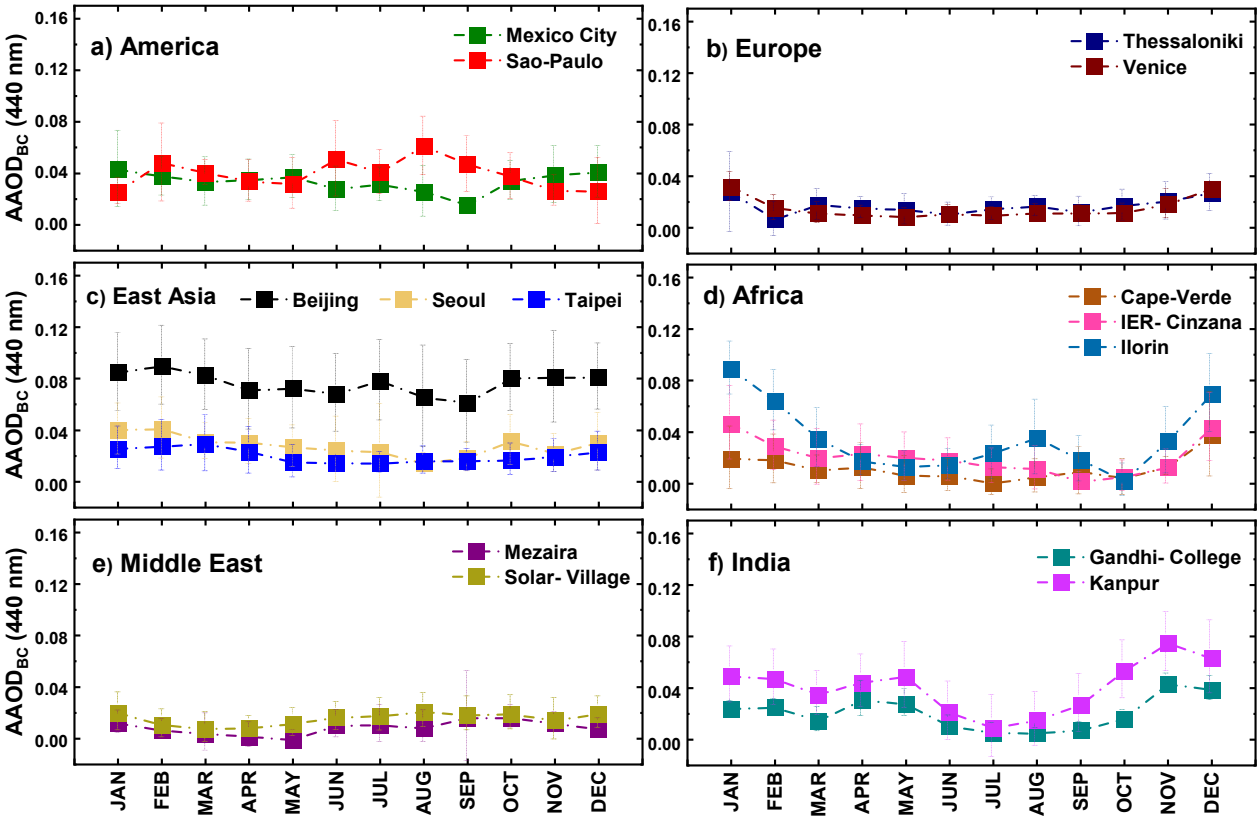

Figure 4. Monthly variations of mean $AAOD_{BC}$ at 440 nm from 2000 to 2018 at fourteen sites. Error bars represent the standard deviation of the monthly averages. (units $AAOD_{BC}$ year^{-1}).

3.2. Annual Variations of BC Ratio ($AAOD_{BC}/AOD_T$ Ratio) and $AAOD_{BC}/AAOD_{Total}$ Ratio

The annual variations of the BC ratio or the ratio of $AAOD_{BC}$ to AOD_T ($AAOD_{BC}/AOD_T$ ratio) at 440 nm during 2000–2018 at the selected sites are shown in Figure 5. Based on the results of the statistical tests, the $AAOD_{BC}/AOD_T$ ratio trends over Thessaloniki, Seoul, Cape Verde, and Kanpur with the Sen's slopes of −0.001, −0.0011, −0.0014, and −0.0011, respectively, are considered significant. The highest inter-annual variability of $AAOD_{BC}/AOD_T$ ratio is particularly evident over Beijing, Mexico City, Sao Paulo, Ilorin, and the Indian sites, approximately higher than 0.04 almost throughout the study period. The least annual BC ratio (less than 0.04) was found over Venice, Cape Verde, and the Middle Eastern sites. None of the Americas sites indicated a significant $AAOD_{BC}/AOD_T$ ratio trend. $AAOD_{BC}/AOD_T$ ratio depicted a significant drop at Thessaloniki (−0.001 year^{-1}) with an elevation in 2008 followed by a decrease from 2009, whereas Venice showed a non-significant steady trend over the study period.

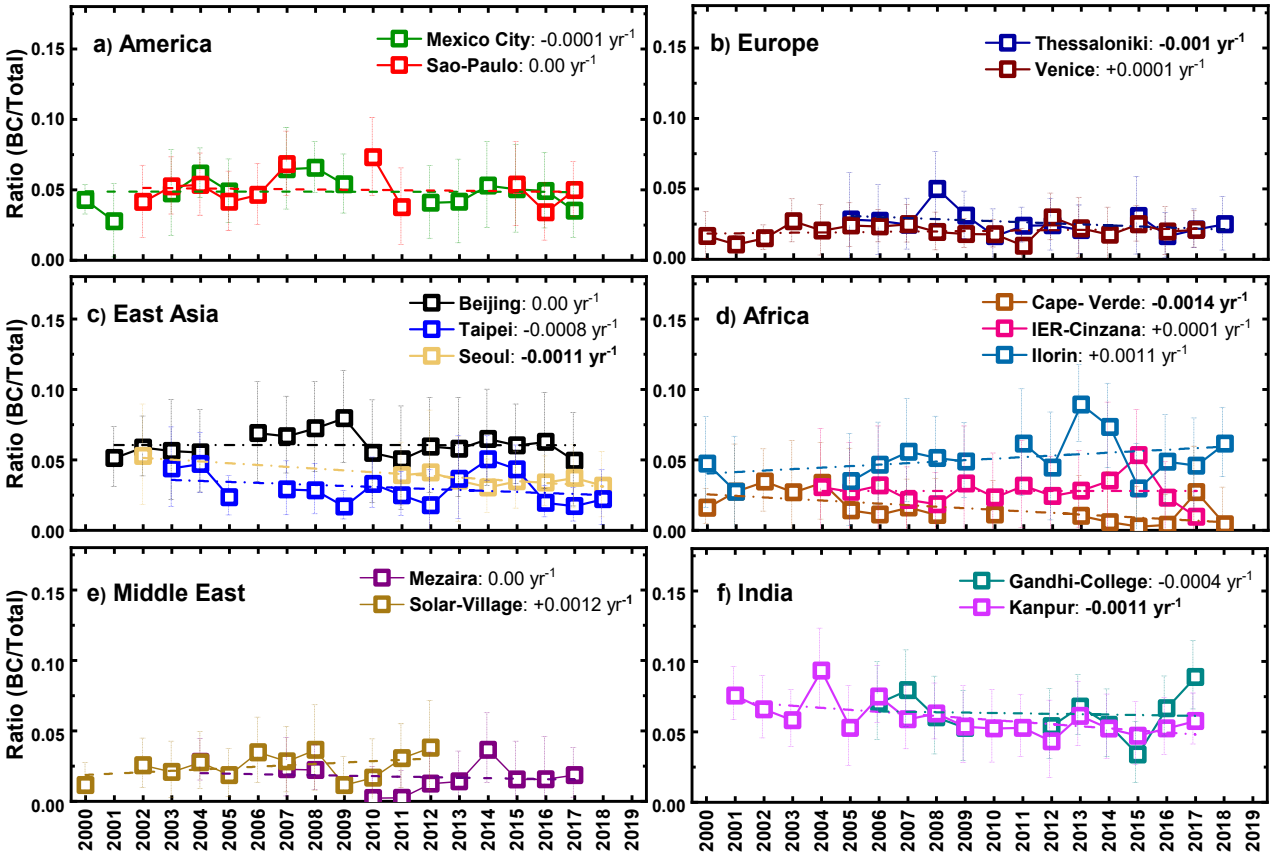

Figure 5. Variations of annual $AAOD_{BC}/AOD_T$ ratio at 440 nm from 2000 to 2018 at fourteen sites. Error bars represent the standard deviation of the annual averages (units year^{-1}).

In the case of the East Asian sites, the highest values of $AAOD_{BC}/AOD_T$ ratio are for Beijing, while Seoul and Taipei showed lower values. A significant decreasing tendency is derived for the Seoul and Cape Verde sites with a declining ratio of -0.0011 year^{-1} and -0.0014 year^{-1}, respectively; Cape Verde indicated the lower $AAOD_{BC}/AOD_T$ ratio (lower than 0.04) compared to the other African sites. There was no significant trend in BC ratio for either of the IER-Cinzana and Ilorin sites; however, a higher BC ratio was found over Ilorin. We found no significant trend for Mezaira during 2000–2018 (note that the data are only available for ten years or less in some sites, including Mezaira and Seoul; thus, it is difficult to ascribe a long-term trend for such sites). In the case of the Indian sites, the $AAOD_{BC}/AOD_T$ ratio trend was only significant in the Kanpur site with the decreasing tendency of -0.0011 year^{-1}, while Gandhi-College revealed no notable trend.

The annual variations of $AAOD_{BC}$ to $AAOD_{Total}$ ($AAOD_{BC}/AAOD_T$ ratio) at 440 nm during 2000–2018 at the selected sites are shown in Figure 6. The statistical tests showed that the $AAOD_{BC}/AAOD_T$ trends are significant over Thessaloniki, Venice, Beijing, Seoul, Taipei, and Cape Verde with the Sen's slopes of -0.015, -0.006, -0.006, -0.018, -0.0094, and -0.0019, respectively. The highest $AAOD_{BC}/AAOD_T$ values were found in Mexico City and Sao Paulo (approximately higher than 0.35); however, none of these sites represented a significant trend. The Americas, European, East Asian, and Indian sites showed higher $AAOD_{BC}/AAOD_T$ than the African and Middle Eastern sites. The least annual $AAOD_{BC}/AAOD_T$ ratio was found over Cape Verde, IER-Cinzana, and the Middle Eastern sites. The $AAOD_{BC}/AAOD_T$ ratio significantly dropped at the European, Cape Verde, and East Asian sites, whereas no considerable trend was found in other sites.

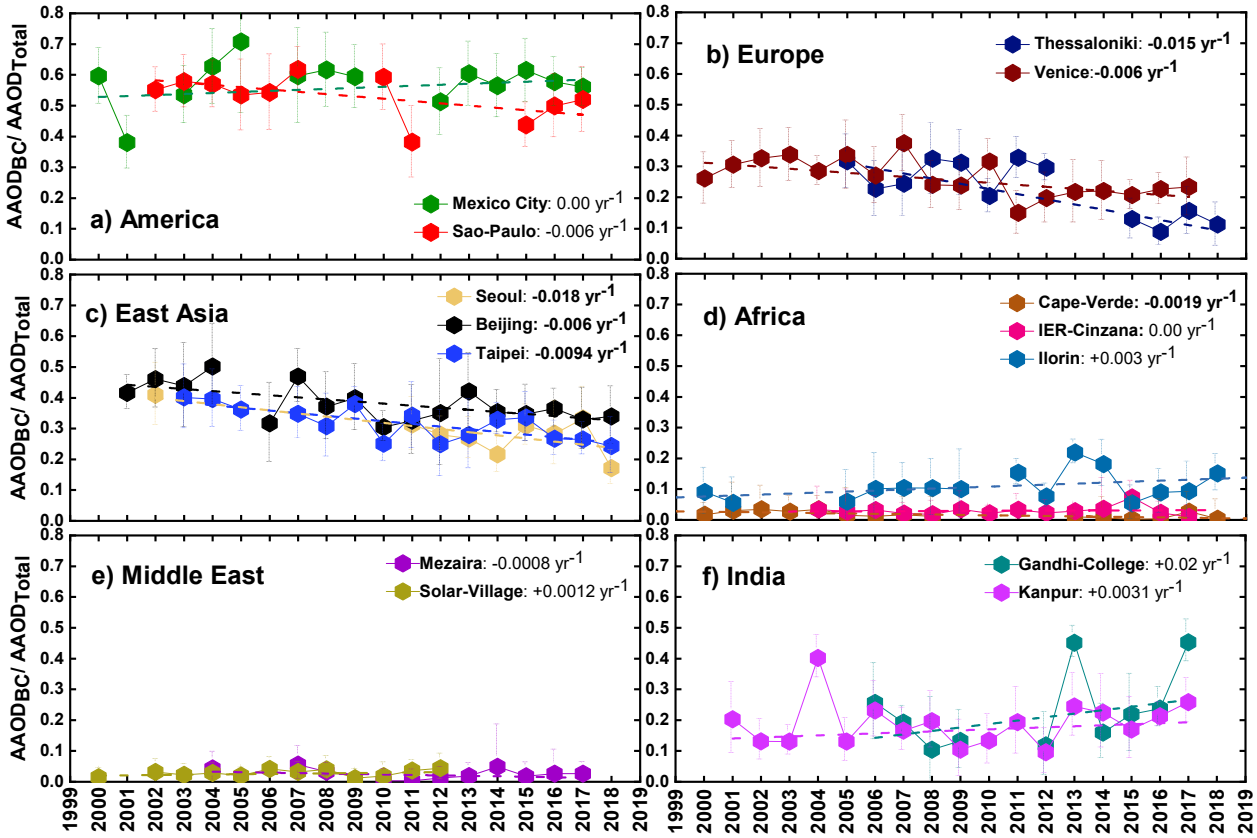

Figure 6. Variations of annual $AAOD_{BC}/AAOD_{Total}$ ratio at 440 nm from 2000 to 2018 at fourteen sites. Error bars represent the standard deviation of the annual averages (units $year^{-1}$).

In the case of the African sites, the highest $AAOD_{BC}/AAOD_T$ value was found in Ilorin, while IER-Cinzana and Cape Verde showed lower values. A significant decreasing tendency is derived for all the East Asian sites; Beijing indicated the highest $AAOD_{BC}/AAOD_T$ ratio compared to Seoul and Taipei. We could not find any significant trend in $AAOD_{BC}/AAOD_T$ ratio for Gandhi College and Kanpur; however, both sites represented a non-significant increasing trend. We found comparable values of $AAOD_{BC}/AAOD_T$ with a non-significant trend over the Middle Eastern sites.

3.3. Correlation between $AAOD_{BC}$ and Coarse- or Fine Mode Particles

To estimate the correlation between $AAOD_{BC}$ and coarse- or fine mode particles, $AAOD_{BC}$ values at each site were compared to total coarse- and fine mode AOD at 440 nm. Figure 7 presents scatterplots of AOD_T and $AAOD_{BC}$ at 440 nm for the fine mode (black circles) and the coarse mode (gray circles) particles at the Americas, East Asian, and African sites. A higher coefficient of determination was found between AOD_T and $AAOD_{BC}$ for the fine mode particles at most sites except for Beijing. For the Americas and East Asian sites, the numbers are 0.15, 0.23, 0.17, 0.08, and 0.31 over Mexico City, Sao Paulo, Seoul, Beijing, and Taipei, respectively. In the case of some sites such as Mexico City, R^2 represented smaller values for both the fine- and coarse mode particles; nonetheless, a higher value was found for fine mode particles over this site. Similar to the American and East Asian sites, we found a higher coefficient of determination between AOD_T and $AAOD_{BC}$ for the fine mode particles at the African sites; the numbers are 0.33, 0.16, and 0.62 over Cape Verde, IER_Cinzana, and Ilorin, respectively. The highest correlation with fine particles was found at Ilorin (R^2 = 0.62).

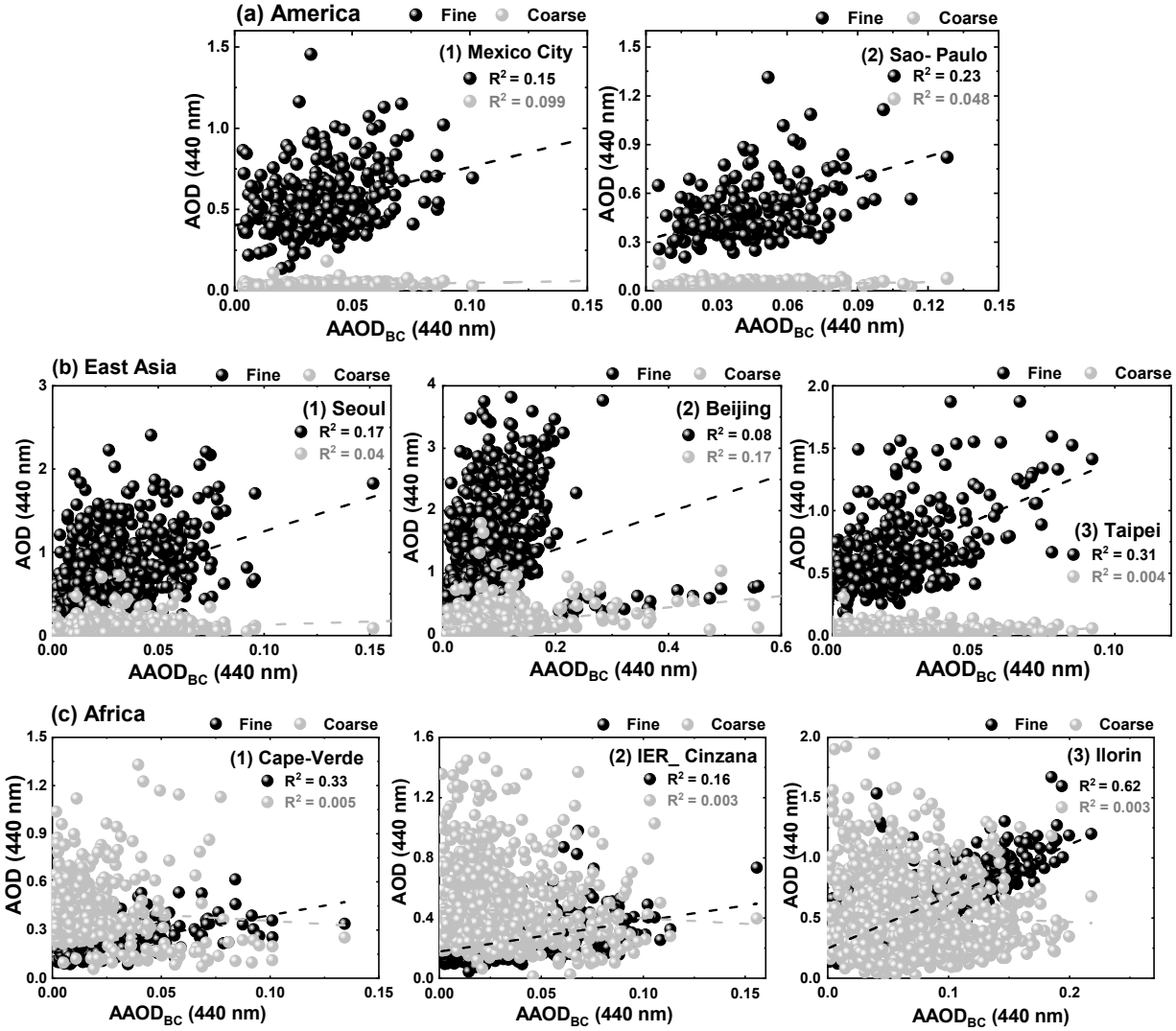

Figure 7. The coefficient of determination (R^2) between $AAOD_{BC}$ and AOD_T at 440 nm for the fine mode (black circles) and the coarse mode (gray circles) at (**a**) the American, (**b**) East Asian, and (**c**) African sites from 2000 to 2018.

The scatterplots of AOD_T and $AAOD_{BC}$ at 440 nm for the fine- and coarse mode particles over Europe, the Middle East, and India are plotted in Figure 8. A higher coefficient of determination was observed between AOD_T and $AAOD_{BC}$ for the fine mode particles at all the European, Middle Eastern, and Indian sites. The values are 0.031, 0.10, 0.12, 0.13, 0.47, and 0.27 for the fine mode over Thessaloniki, Venice, Mezaira, Solar-Village, Kanpur, and Gandhi-College, respectively. Similar to Mexico City, R^2 indicated smaller values for both the fine- and coarse mode particles over Thessaloniki; nevertheless, a higher correlation was found for fine mode particles over this site as well. $AAOD_{BC}$ exhibited the highest correlation with fine mode particles over Kanpur (R^2 = 0.47); also, higher dependence on fine mode particles was identified over Gandhi Collage (R^2 = 0.27) compared to the other sites.

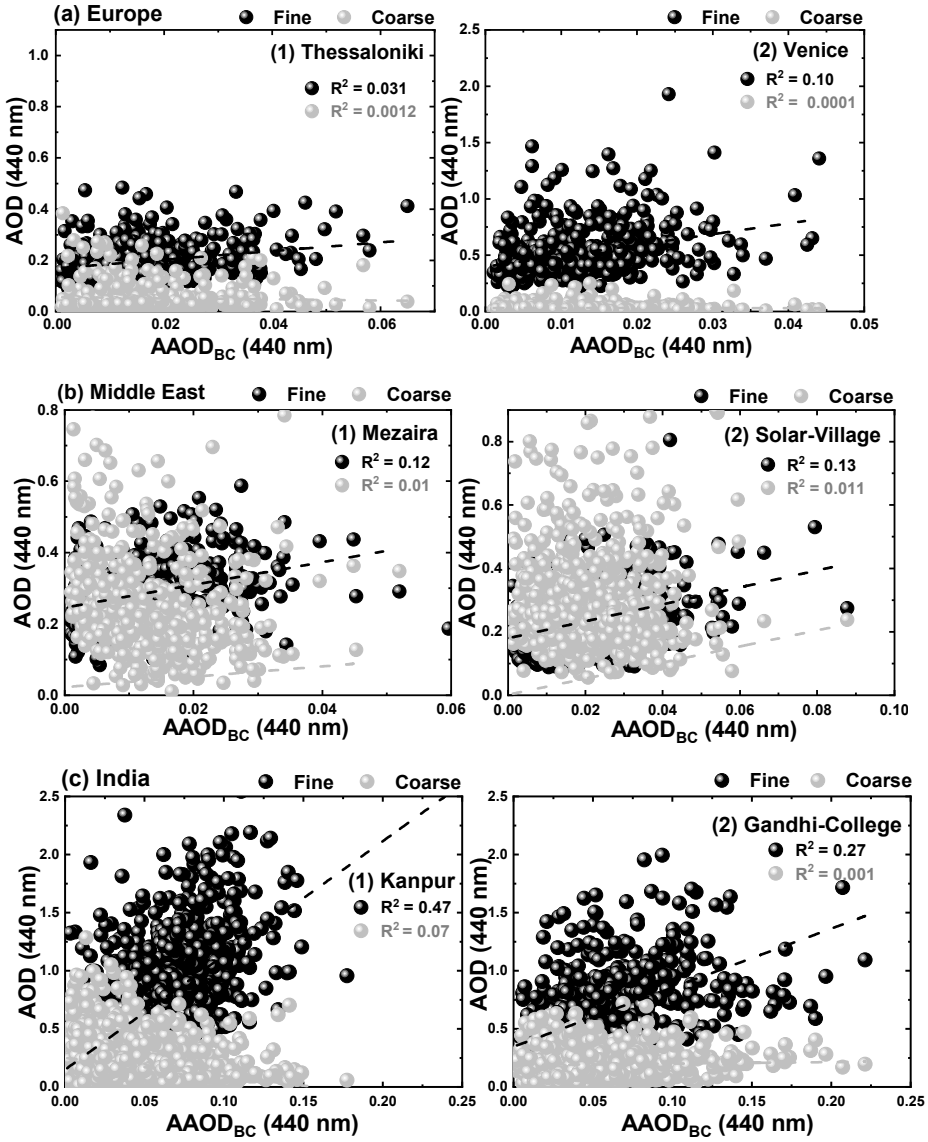

Figure 8. The coefficient of determination (R^2) between $AAOD_{BC}$ and AOD_T at 440 nm for the fine mode (black circles) and the coarse mode (gray circles) at (**a**) the European, (**b**) Middle Eastern, and (**c**) Indian sites from 2000 to 2018.

3.4. Uncertainties in $AAOD_{BC}$ Retrieval Methodology

To assess the uncertainties in $AAOD_{BC}$ retrieval methodology, we calculated the CI of $AAOD_{BC}$ at each site from 2000 to 2018. The highest and lowest CI for $AAOD_{BC}$ is related to Beijing with the value of ± 0.02 and the Middle eastern sites with the value of ± 0.004, respectively. For the Indian, Americas, and European sites, the values are ± 0.01, ± 0.008, and ± 0.005, respectively. Similar to the European sites, IRE-Cinzana and Taipei with the CI of ± 0.005 showed lower values; however, the higher CIs were found over Seoul, Ilorin, and Cape Verde (± 0.007, ± 0.016, and ± 0.008, respectively).

4. Discussion

4.1. Annual Mean AOD_T

According to Figure 2, a significant declining trend in AOD_T was found over Mexico City, Thessaloniki, Venice, and Beijing, while Kanpur represented an upward trend during 2000–2018. The variations found in AOD_T agree with the results of a previous study by Li et al. [41], which reported the same decline in AOD over Venice, Beijing, Cape Verde, IER-Cinzana, and Ilorin, and also a similar upward trend in Solar Village and

Kanpur from 2000 to 2013. The tendencies found over North and South America, Europe, and some parts of Africa are compatible with the results of the preceding studies based on satellite-based AOD; however, the AOD growing trend over Arabian Peninsula is in harmony with simulation model results due to the lack of satellite information over bright surfaces [42]. The higher annual mean AOD over Ilorin than in other semi-arid locations could be attributable to the influence of dust and anthropogenic sources [43]. In southern Africa, biomass-burning emissions contribute an estimated 86% of total carbonaceous aerosols generated in Africa, a high percentage compared to the other regions worldwide. Moreover, Africa is known as the largest individual source of dust and biomass-burning emissions globally [44]. Biomass-burning aerosols make up a significant fraction of AOD_T at the Ilorin site [45]. The AOD_T at Cape Verde is influenced by dust particles transported from the Saharan desert and carbon particles resulting from biomass-burning in the region south of the Sahel and local traffic emissions [46]. In the case of the Middle Eastern sites (e.g., Mezaira and Solar Village) located in arid areas, major dust outbreaks and storms highly affect air quality by transferring airborne particles and hence significantly contribute to the overall AOD over these regions. Natural dust and a large amount of finely ground sand are the main drivers of the increase in AOD; moreover, the use of natural resources of fossil fuels (largely oil reserves) and related industries, and particulate matter (PM) emitting from construction sites are some other causes of AOD variations over this region [47].

Based on satellite-retrieved data, Alpert et al. [48] found a decline in the AOD over Mexico City and Sao Paulo during 2002–2010. Similar to our findings, Carabali et al. [49] showed that the mean AOD at 500 nm over Mexico City was nearly half of the maximum values measured at Chinese urban sites during 1999–2014. In other literature, the highest AOD daytime variation at 440 nm was occurred in Mexico City compared to Sao Paulo [50]. The higher AOD_T over Mexico City and Sao Paulo is partly attributable to the higher population of these sites. Mexico City is the most populous city in North America. In 2020, the population for the city itself was approximately 9 million people, but when looking at the entire metropolitan area, this number rises to ~21 million. Vehicles are the primary source of air pollution in Mexico City; emissions from the exhaust of these automotive fleets contain hydrocarbons (fossil fuels), carbon monoxide, and nitrogen oxides that are released into the atmosphere in considerable quantities. Another factor in the higher AOD_T over Mexico City is the geographical location of this city [51]. As Mexico City is located in a valley (valley of Mexico), when the speed of the winds is low, the diffusion of pollutants is minimum; for at least seven months a year, the region maintains, on average low-speed winds. In addition, the role of altitude in the high rate of pollution over this region should not be ignored; since Mexico City's altitude is high, the low oxygen quantity results in deficiencies in the combustion processes of the engines and higher air pollution over this city. Sao Paulo is the most populous city in Brazil and the continent. As seen in many populated cities worldwide, vehicular emissions appear to be the most prominent source of air contamination and high AOD over Sao Paulo [52]. Particles released from construction sites, the combustion of wood or plants in any form of the open burning site (for cooking or similar activities), and emissions from factories are considered as the other sources of high AOD at Sao Paulo.

A decrease in AOD over Venice, Thessaloniki, and North America from 2000 to 2009 was observed previously, mainly due to decreasing emissions of SO_2, NO_x, and other pollutants [53]. The reduction in AOD over Europe coincides with the implementation of air quality regulations to minimize the emission of SO_2 and other atmospheric aerosols from 1990, which improved air quality. It has been reported that the drop in AOD trend over Europe and America is mainly due to the decrease in emissions, while meteorological changes are the main drivers of AOD changes over the Middle East and Africa [41,42].

In contrast to the declining emission trends over Europe and North America, anthropogenic emissions have been escalating in South Asia in recent decades. We found an upward AOD trend in Kanpur that is consonant with previous studies based on ground-based measurements and satellite observations [54]. As India is one of the most polluted

countries and is projected to be the most populous country in the world in the coming decades, the high AOD and its upward tendency are expected. About 40 cities in India are identified as "high-pollution" areas with annual mean PM_{10} levels of 61–90 $\mu g/m^3$, and 85 cities are considered as "critical", exceeding the PM_{10} standard by over 1.5 times [55]. The high AOD over the Indian sites, particularly Kanpur, is attributable to dust aerosols (and mixed types of aerosols) as the main component during the monsoon season and anthropogenic emissions during winter and post-monsoon seasons over this metropolis city [56]. More than 75% of total AOD over Kanpur is attributable to fine mode urban/industrial aerosols during winter [57].

The high AOD over Beijing primarily results from anthropogenic activities associated with secondary aerosol formation and natural aerosol flux (such as sea salt and dust), large population, and urbanization [58]. Since the beginning of industrialization, Beijing has suffered poor air quality due to the high emissions of sulfate, carbonaceous, and other aerosols from growing fuel consumption. The rapid increase in AOD from 2000 to 2006 and a gradual decrease from 2006 to 2014 over Beijing was previously reported, mainly due to anthropogenic emissions over this city [59]. Moreover, long-range transported natural and anthropogenic aerosols generated in China affect the air quality and AOD_T over downward areas, e.g., Seoul, due to prevailing westerlies over East Asia. Dust plumes transported from deserts in China and Mongolia affect the air quality in China and downwind regions such as Taipei and Seoul, particularly during the spring season [60]. The downward trend of AOD in Beijing can be due to improving air pollution control measures and the implementation of strict government policies to control air pollution in this country [61]. The lower variation of annual mean AOD at Seoul and Taipei is associated with lower air pollution emissions at these sites compared to China.

4.2. Annual and Monthly Mean $AAOD_{BC}$

Based on Figure 3, the higher $AAOD_{BC}$ was observed over Beijing, Ilorin, Mexico City, Sao Paulo, and the Indian sites, with the maximum values in Beijing and Ilorin from 2000 to 2018. Besides, $AAOD_{BC}$ declined significantly over Sao Paulo, Thessaloniki, Beijing, Seoul, and Cape Verde during the study period. Sun et al. [14] reported a downward tendency in $AAOD_{BC}$ during 2008–2017 over China, with a considerable influence on AAOD over this area. A decreasing trend in BC concentration over Beijing was reported in other studies, which might explain the downward tendency of $AAOD_{BC}$ over this region [62]. Restrictions on gasoline and coal consumption (both local and industrial), traffic regulations, government's air pollution actions (e.g., Multi-resolution Emission Inventory version 1.3 (MEIC1.3) and Regional Emission inventory in Asia (REAS)) appear to be the main drivers of BC reduction in China [63]. The high $AAOD_{BC}$ in China largely results from industrial and local carbon-containing pollutants associated with population density and economic growth over the recent decades. Transportation and liquid fuels such as gasoline and diesel have been found to play an important role in BC emission over Beijing [64].

The contribution of BC to AAOD was previously compared at polluted urban regions of Seoul and Beijing and background sites [65]. It has been found that BC made a more outstanding contribution to AAOD in the polluted urban regions than the background sites. The contribution of BC to AAOD is estimated to be 84.9 $\pm$ 2.8% in polluted urban cities, while BrC's contribution is lower (15.1 $\pm$ 2.8%). In Seoul, we found a decreasing tendency in $AAOD_{BC}$ (higher than 0.04 before 2002 and lower than 0.04 after 2011). In 2002, the government began attaching diesel particulate filters (DPF) to old diesel mobiles and supplying compressed natural gas (CNG) buses in Seoul. Moreover, Seoul started the disposal of old diesel vehicles in 2003. Since 2005 regulations on air pollutants emitted from diesel engines have been strengthened in this metropolitan area. Therefore, the significant decreasing trend in $AAOD_{BC}$ in Seoul, particularly after 2002, might be highly affected by these diesel mobile-related policies and reduction in emissions from diesel engines over this city. $AAOD_{BC}$ variations in Seoul are driven predominantly by local anthropogenic emissions but are influenced by industrial emissions in the west and emissions from

biogenic, agricultural, and biomass burning sources in the east of the Seoul metropolitan area as well. Furthermore, $AAOD_{BC}$ in Seoul can be impacted by the long-range transport of anthropogenic particles. For instance, as Seoul is located in the central west of the Korean Peninsula facing the yellow sea in the west, $AAOD_{BC}$ in Seoul is highly influenced by continental outflows from the Asian continent (such as China). $AAOD_{BC}$ variations over Taipei are mainly attributable to local and transported BC emissions. BC contribution to the total AOD in Taipei is estimated to be 1.5% on average. Over 90% of the total BC in Taipei results from the BC emissions from anthropogenic sources in Asia. North-East and South-East Asia are considered as the prominent source regions of various anthropogenic aerosols to Taipei, accounting for 51% and 34.2% of total black carbon on annual average, respectively [66]. The corresponding share of BC from anthropogenic emissions in North-East Asia demonstrates a higher contribution during the winter season. However, the contribution of South-East Asia in the total BC in Taipei is more pronounced in summer.

Mexico City and Sao Paulo, with a population of ~9 and 12 million inhabitants, respectively, represented higher $AAOD_{BC}$ than other sites such as Venice or the Middle Eastern sites. A higher absorption coefficient related to BC was reported over Mexico City and nearby, likely associated with vehicular activities, local fires, and biomass-burning [67]. Sao Paulo is one of the most congested cities globally, and traffic is the principal source of BC emissions (mainly emitted from heavy vehicles) in this city. Sao Paulo metropolitan area with almost 8 million motorized vehicles and 100-km-long traffic jams has high concentrations of air pollutants, particularly in the winter season. High BC emissions from diesel (around four times) and gasoline vehicles are the leading sources of elevated BC concentration and $AAOD_{BC}$ over Sao Paulo [68]. The significant decreasing trend in $AAOD_{BC}$ at Sao Paulo may result from the following governmental actions: decentralization of economic activities to the surrounding areas, construction of a ring road around the metropolitan area (Rodoanel), improvement of public transportation, expansion of subway line networks, setting air quality and emission standards, and control measures implemented by the local and state government in Sao Paulo to reduce the emission of BC, carbon monoxide (CO), volatile organic compounds (VOC), and toxic pollutant in the past years [69].

We found one of the highest annual mean $AAOD_{BC}$ values at the Ilorin site in Nigeria, one of the world's leading gas flaring nations. Gas flaring is a daily routine in this region known as a considerable BC (soot), CO, and VOC source. The Ilorin AERONET site is located to the north of the gas flaring region in Nigeria, with over 300 active flare sites and an estimated annual average volume flared of 15 billion cubic meters, which can considerably contribute to the high $AAOD_{BC}$ over this region [70]. Hence, regardless of the high BC emission at this site, Ilorin's AERONET site location plays a prominent role in the high $AAOD_{BC}$ variations over this site. In addition, volcanic ash, fossil fuel combustion, and power backup generators powered by fossil fuels contribute to BC emissions over Nigeria.

Ramachandran and Rajesh. [71] showed that BC mass concentration over India, Beijing, and Seoul are higher than those measured over European and American sites. Whilst BC emissions are reported to be declining in the US and across Europe [72], they are rising in much of the world. BC emissions in the European Union (EU; including Italy and Greece) to a large extent originate from the residential sectors and transportation [73]. Diesel engines have been a specific target in urban areas due to their enormous (90%) contribution to the transport share of BC emissions [74]. The EU legislation on controlling BC emissions associated with Arctic climate warming could be the potential motivation for the declining and the constant trend of $AAOD_{BC}$ over Thessaloniki and Venice, respectively. Moreover, other regulations and mitigation policies such as tighter vehicle emission testing standards and schemes to reduce diesel cars in cities were likely the other reasons the $AAOD_{BC}$ decreased over the US and Europe during the past twenty years.

In India, coal-burning is a prominent source of energy that supplies 76% of the country's requirements, and it is a significant source of BC mass concentration into the environment [75]. In addition, biofuel burning, agriculture fires, and vehicular emissions due to the high population are the other major sources of BC aerosols over the Indo-Gangetic

Basin (IGB) areas [76]. Wood and biomass burning for cooking and heating drive up the BC emission over India, not only in urban areas but also in rural areas. As Kanpur and Gandhi-College are located in urban areas with high populations, $AAOD_{BC}$ showed almost similar variations for both sites. In India, the traffic sector (specifically the motorbikes) emits large quantities of BC due to incomplete combustion. Furthermore, coal burning in the power plants might constitute the significant sources of BC emissions in Kanpur and Gandhi College. A considerable fraction of aerosols over India are light-absorbing and contain BC; hence, they are expected to lead to a higher $AAOD_{BC}$ in this region [77]. BC emissions conjoined with dust loads from local sources were found to have the power to change the rainy period during late spring over northern India.

Although the AOD_T variation over the Middle Eastern sites represented roughly high values, $AAOD_{BC}$ showed lower values over these sites, implying the more significant role of natural aerosols and dust outbreaks in air pollution than anthropogenic pollution or carbon-containing particles in the Middle East. Variations in $AAOD_{BC}$ over Mezaira are mainly influenced by BC sources, including the petrochemical industry and maritime shipping (transferred from the coastal area of Abu Dhabi). Moreover, electricity generation and industrial activities such as fertilizer use and water desalination plants are found to be the other sources of BC emissions over this region, specifically in Solar Village [78].

According to Figure 4, the $AAOD_{BC}$ at Beijing, Sao Paulo, Mexico City, and the Indian sites exhibited a seasonal pattern; an increase in $AAOD_{BC}$ over the cold months and lower values during summertime. The seasonal dependence of $AAOD_{BC}$ emphasizes the role of domestic heating in BC emissions related to coal-based fuels over these sites. Several studies have reported similar seasonal variations in BC variations over China [79]. Liu et al. [80] reported a general decrease in BC concentration during 2002–2014 in Beijing, with the highest average concentration in winter associated with extensive coal consumption and meteorological conditions. We found slightly higher $AAOD_{BC}$ in July than the other warm months over Beijing, more likely associated with biomass-burning sources in the summertime [81]. The increased AAOD in China and Korea during winter is attributable to the elevation of BC and OC emissions in response to incomplete combustion of fossil fuel for domestic heating [82].

Local heating is a significant source of BC during the winter season in Sao Paulo and Mexico City, while primary emissions by motor vehicles are dominant throughout the year, regardless of the seasons [83]. Besides, most of the rainfall in Mexico City occurs from Jun to September, when low-pressure systems over the Atlantic and Pacific oceans convey air masses loaded with moisture which causes rainfall over the country and lowers the atmospheric pollution during this period. We found lower $AAOD_{BC}$ from March to November over Ilorin, with the minimum value in October and a peak in August. Ilorin experiences a rainy season from April to October with a peak in October, while the dry season lasts for almost five months, from November to March, with the slightest chance of a rainy day (1%) at the end of December. Therefore, the lower $AAOD_{BC}$ during the wet months (minimum in October) and higher values over dry months (maximum during December–January) is partly attributable to the rainfall that lowers atmospheric pollution load during the wet months. $AAOD_{BC}$ peaks during late fall to early winter at the Ilorin site (peaking at ~0.09 in January). This coincides with the sub-Sahelian biomass-burning season (December–February) over northern Africa, influencing $AAOD_{BC}$ variations over Ilorin. The highest AOD during December-February out of the western African sites affects Ilorin, which is closer to the primary area of biomass-burning during this time [45]. Savanah, grassland fires, and biomass-burning are the significant sources of BC during the dry seasons over Africa; however, residential heating during winter is considerable [84].

The seasonal variation in $AAOD_{BC}$ is less pronounced over Europe than in Beijing, the Americas, and the Indian sites. The contribution of fossil fuel in BC concentration is more evident in summer over Greece, and however wood burning contributes considerably to BC concentration in wintertime [85]. Bikkina et al. [86] found the highest total carbon-based fraction biomass in fall and winter (October to February) and lowest values in

summer (June−September) over Kanpur. The carbonaceous aerosols in winter and fall are affected by transport of crop residue burning and wood combustion emissions in the northern Indo-Gangetic Plain (IGP); however, local sources (wheat residue combustion and vehicular emissions) were identified as the dominant sources in spring and summer. $AAOD_{BC}$ variations over the Middle East and Taipei indicated slightly higher values during wintertime and from June to August only over the Middle Eastern site. Since the winter season in Taipei, Saudi Arabia (the Solar-Village site), and the United Arab Emirates (the Mezaira site) is mostly mild and moderate, we concluded that the residential heating contribution in the elevation of $AAOD_{BC}$ in winter might be slightly over these sites and-or the sources of BC are identical throughout the year.

4.3. Annual Mean BC Ratio ($AAOD_{BC}/AOD_T$ Ratio) and $AAOD_{BC}/AAOD_{Total}$ Ratio

Figure 5 represents the variations of the annual ratio of $AAOD_{BC}$ to AOD_T ($AAOD_{BC}/AOD_T$) or BC ratio and their trends for 2000–2018. A significant declining trend was found over Thessaloniki, Seoul, Cape Verde, and Kanpur. The BC ratio indicated higher values over Sao Paulo, Mexico City, Beijing, Ilorin, and the Indian sites (higher than 0.04) owing to the higher BC concentrations over these sites compared to the other sites. Despite the significant decrease in AOD_T in both European sites, the BC ratio declined only over Thessaloniki; however, the BC ratio in Venice remained stable or increased during 2000–2018. This revealed that the decrease in aerosol load over Venice largely results from the decrease in emission of other aerosol species. The highest values of the BC ratio were found over Beijing, Ilorin, and Sao Paulo, indicating the notable contribution of BC in air pollution compared to the other particles. A significant downward tendency in BC ratio over Thessaloniki mainly results from the decline in BC emission during 2003–2011. Therefore, it can be concluded that Thessaloniki's decline in BC emissions was higher than that at the Venice site. The greater significant decline in AOD_T trend over Beijing compared to $AAOD_{BC}$ and the non-significant tendency in BC ratio implies the decline in all aerosol types added to BC emissions decline over Beijing. The notable decline in BC ratio over Kanpur in contrast to the upward tendency in AOD_T over this site signifies the important role of BC in air pollution over Kanpur; however, the contribution of other aerosols in elevation of AOD_T should not be ignored. The decline in BC ratio and $AAOD_{BC}$ over Cape Verde compared to the other African sites (with the non-significant upward trend) indicates the faster reduction in BC emissions over this site.

Figure 6 shows the variations of the annual $AAOD_{BC}$ to $AAOD_{Total}$ ratio ($AAOD_{BC}/AAOD_T$) and their trends during 2000–2018. The $AAOD_{BC}/AAOD_T$ indicated higher values over the Americas, East Asia, Europe, and India, with the highest values over Sao Paulo and Mexico City. The $AAOD_{BC}/AAOD_T$ represents the ratio of $AAOD_{BC}$ to total AAOD (here, total AAOD is considered AAOD induced by BC, dust, and BrC), expressing the proportion of BC in light-absorbing aerosols. Therefore, the high variations of $AAOD_{BC}/AAOD_T$ imply the increased contribution of BC in light absorption compared to other light-absorbing aerosols over the Americas, East Asia, India, and Europe. The highest $AAOD_{BC}/AAOD_T$ over Mexico City and Sao Paulo indicates the increased portion of BC in light absorption compared to other light-absorbing aerosols (i.e., dust and BrC) over these populous cities. The lower $AAOD_{BC}/AAOD_T$ despite the high $AAOD_{BC}$ over Beijing might be attributable to the high contribution of dust (transferred from China and Mongolia deserts) and BrC in light absorption, which lowered the $AAOD_{BC}/AAOD_T$. Like Beijing, as the Ilorin site is highly affected by the Saharan dust, $AAOD_{BC}/AAOD_T$ indicated lower values, despite the higher $AAOD_{BC}$ and AOD_T, emphasizing the high proportion of dust in light absorption along with BC. In the case of the European sites, Taipei, and Seoul, since none of these sites are adjacent to the deserts, the proportion of dust in light absorption seems lower than BC. Although these sites are influenced by dust transportation from other deserts, the dust influence is lower than the African, Middle Eastern, and Beijing sites. Therefore, the high variations in $AAOD_{BC}/AAOD_T$ (despite lower $AAOD_{BC}$) highlight BC's more prominent role in light absorption than dust and BrC.

The very low $AAOD_{BC}/AAOD_T$ over the Middle East, Cape Verde, and IER-Cinzana might denote the significant contribution of other light-absorbing aerosols (particularly dust) in light absorption than BC. The significant decreasing tendency in $AAOD_{BC}/AAOD_T$ over the European, Cape Verde, and East Asian sites implies the reduction of BC's share in light absorption compared to the past. In other words, BC proportion in light absorption compared to other light-absorbing aerosols seems to be decreased from 2000 to 2018 over the European, Cape Verde, and East Asian sites.

Table 4 summarizes the results of our $AAOD_{BC}$ retrieval methodology and compares them with previous research results.

Table 4. Comparison of our $AAOD_{BC}$ retrieval methodology results with previous research.

Our Approach	Previous Studies
A Downward trend in $AAOD_{BC}$ at the Beijing site from 2001 to 2017	A downward tendency in $AAOD_{BC}$ was found over China during 2008–2017, with a considerable influence on AAOD over this area [14]. A decreasing trend in BC concentration was reported over Beijing [62].
Higher $AAOD_{BC}$ and $AAOD_{BC}/AAOD_T$ over the Americas imply the high contribution of BC in light absorption.	A higher absorption coefficient related to BC was reported over Mexico City [67]. Elevated BC concentration was reported due to the high BC emissions over Sao Paulo [68].
Lower $AAOD_{BC}$ over the European sites than the other sites	The European and American sites showed lower BC mass concentration than India, Beijing, and Seoul [71].
Higher variations in $AAOD_{BC}$ over the Indian sites	A considerable fraction of aerosols over India were found to be light-absorbing which contain BC [77].
Higher $AAOD_{BC}$ and $AAOD_{BC}/AAOD_T$ at the Ilorin site, indicating the high contribution of BC and dust in light absorption at this site.	The higher annual mean AOD was found over Ilorin mainly attributable to the influence of dust and anthropogenic sources [43].

4.4. Correlation between $AAOD_{BC}$ and Coarse- or Fine Mode Particles

We found a higher coefficient of determination between AOD_T and $AAOD_{BC}$ for the fine mode particles over all the American, African, Indian, European, Middle Eastern, and East Asian sites except for Beijing. R^2 exhibited smaller values for both the fine- and coarse mode particles over Thessaloniki; however, a relatively higher correlation was found for fine mode particles at these sites as well. Freshly emitted BC particles in the atmosphere are primarily of anthropogenic origin and in fine mode [87]; therefore, the BC's higher correlation with fine mode particles is expected. Ynoue and Andrade [88] concluded that fine mode particles receive a greater contribution from carbonaceous particles over Sao Paulo. Different BC sources from fossil fuel and biomass-burning aerosols have different BC particle size distributions, which may explain the lower and/or various correlations over different sites in this study [89,90]. On the other hand, BC particles exist in the form of aggregates with small carbon spherules and spherical monomers [91]. In addition, aging can lead to BC particles mixing with other coarse aerosols such as dust, sea salt, and sulfate [92]. Urban BC particles tend to have smaller sizes, fewer coated, and thinner coatings than biomass-burning BC particles [93]. The major fraction of the organic carbon aerosol associated with biomass-burning emission is water-soluble, which might affect the optical size of biomass-burning BC [94]. Wang et al. [95] found a significant contribution of primary fossil fuel and biomass-burning organics (64% of total organics) over Beijing. The authors confirmed that secondary species might have considerable impacts on the properties of BC-containing particles, particularly for ones with larger BC core sizes and thicker coating. The higher correlation of $AAOD_{BC}$ and coarse mode particles might result from the BC particle aggregation with the other secondary species, specifically over the highly polluted areas in Beijing. Besides, more polluted periods would have more

contribution from other pollutants, and more thickly coated BC tends to associate with other species. This fact emphasizes the notable role of chemical aging in the pollution of BC particles during the long-term pollution episode in Beijing, particularly within the first decade of our study. As was reported by Zhao et al. [96], BC rapidly accumulates and becomes more homogenously mixed and represents a larger core size during pollution episodes in Beijing. Moreover, due to the high concentration of gas precursors and pre-existing particles during high pollution episodes, BC has more chance to be thickly coated. Overall, aging, BC emission from different sources, BC aggregation properties seem to be the main drivers of higher $AAOD_{BC}$ correlation with coarse particles over Beijing.

4.5. $AAOD_{BC}$ Methodology Assessment

The uncertainties in $AAOD_{BC}$ retrieval using this methodology mainly arise from AERONET-retrieved AODs and ω. The highest uncertainty in $AAOD_{BC}$ retrieval for this methodology was found in Beijing ($\pm$0.02); however, the Middle Eastern sites indicated the lowest values ($\pm$0.004).

5. Conclusions

In this study, we presented the long-term variations of AOD_T, $AAOD_{BC}$, the ratio of $AAOD_{BC}/AOD_T$, $AAOD_{BC}/AAOD_{Total}$, and $AAOD_{BC}$ correlation with fine- or coarse mode particles retrieved from AERONET measurements over North and South America, Europe, East Asia, Africa, the Middle East, and India. To the best of our knowledge, fewer studies have investigated the aerosol optical properties, BC light absorption, and their trends for the long-term on a continental scale. Therefore, this study serves as a reference for evaluating the decadal BC variations globally. The major findings and conclusions are summarized as follow:

- A significant declining trend in AOD_T was found over Mexico City, Beijing, and the European sites, while Kanpur represented an upward tendency during 2000–2018. The highest AOD_T was observed over Sao Paulo, Beijing, Ilorin, and the Indian sites. The upward tendency in AOD_T over Kanpur might be attributed to dust, mixed aerosols, and anthropogenic urban-industrial emissions mainly associated with the high population over this metropolitan city. The downward tendency in AOD_T over China, Europe, and America might be related to the decrease in emissions and the governmental air pollution control policies over these areas.
- Higher $AAOD_{BC}$ was observed over Beijing, Ilorin, Mexico City, Sao Paulo, and the Indian sites, with the maximum values in Beijing and Ilorin. $AAOD_{BC}$ declined significantly over Sao Paulo, Thessaloniki, Beijing, Seoul, and Cape Verde. High population, local and industrial emissions, transportation, and carbon-containing fuel consumption for house warming could be the main drivers of higher $AAOD_{BC}$ over Beijing, Mexico City, Sao Paulo, and the Indian sites. In contrast, $AAOD_{BC}$ variation over Ilorin is significantly affected by biomass burning, agriculture fires, and other emission sources.
- We found that besides the local anthropogenic emissions, the $AAOD_{BC}$ variations are also influenced by other factors such as the site's geographical location, altitude, the local diffusion condition, wind speed, and precipitation.
- The $AAOD_{BC}$ at Beijing, Sao Paulo, Mexico City, and the Indian sites showed a clear seasonality with an increase over the cold months and lowered values during summertime. The seasonal dependence of $AAOD_{BC}$ emphasizes the notable role of residential heating in BC emissions related to coal-based fuels over these sites.
- We found a higher coefficient of determination between AOD_T and $AAOD_{BC}$ for the fine mode particles at all sites except for Beijing. This higher correlation can be attributed to the fact that BC particles in the atmosphere are mostly of anthropogenic origin and in fine mode. We concluded that aging, BC emission from different sources, BC aggregation properties might be the leading cause of higher $AAOD_{BC}$ correlation with coarse particles over Beijing.

Finally, although the $AAOD_{BC}$ changes were derived in various sites, additional sites and studies are needed to provide a more precise global conclusion and better understand the causes for BC variations. Therefore, in our future work, we plan to add more sites to our current sites and better conclude the $AAOD_{BC}$ variations worldwide.

Author Contributions: Writing—original draft, N.D.; Conceptualization, Y.N.; Data curation, S.J., N.D., and S.S.; Formal analysis, N.D.; Software, N.D. and J.S. All authors have read and agreed to the published version of the manuscript.

Funding: This work was supported by the "Graduate School of Particulate Matter Specialization" of Korea Environmental Industry & Technology Institute grant funded by the Ministry of Environment, Republic of Korea, and by the National Research Foundation of Korea (NRF) grant funded by the Korean government (MSIT, MOE) and (Grant No. 2019M3E7A1113103).

Institutional Review Board Statement: Not applicable.

Informed Consent Statement: Not applicable.

Data Availability Statement: The data used in this work are freely available through the AERONET portal at https://aeronet.gsfc.nasa.gov/ (accessed on 15 March 2021).

Acknowledgments: We would like to gratefully thank the principal investigators of the AERONET sits used in this study for instrument maintenance and providing their data to the community.

Conflicts of Interest: The authors declare no conflict of interest.

Abbreviations

$AAOD_{BC}$	Black Carbon Absorption Aerosol Optical Depth
$AAOD_{BrC}$	Brown Carbon Absorption Aerosol Optical Depth
(DPR, δ^{P})	Depolarization Ratio
(SSA, ω)	Single Scattering Albedo
(AE, å)	Ångström Exponent
R_d	Dust Ratio

References

1. Curci, G.; Alyuz, U.; Barò, R.; Bianconi, R.; Bieser, J.; Christensen, J.H.; Colette, A.; Farrow, A.; Francis, X.; Jiménez-Guerrero, P.; et al. Modelling black carbon absorption of solar radiation: Combining external and internal mixing assumptions. *Atmos. Chem. Phys.* **2019**, *19*, 181–204. [CrossRef] [PubMed]
2. Samset, B.H.; Stjern, C.W.; Andrews, E.; Kahn, R.A.; Myhre, G.; Schulz, M.; Schuster, G.L. Aerosol Absorption: Progress Towards Global and Regional Constraints. *Curr. Clim. Chang. Rep.* **2018**, *4*, 65–83. [CrossRef] [PubMed]
3. Pani, K.S.; Wang, S.; Lin, N.; Chantara, S.; Lee, C.; Thepnuan, D. Black carbon over an urban atmosphere in northern peninsular southeast Asia: Characteristics, source apportionment, and associated health risks. *Environ. Pollut.* **2020**, *259*, 113871. [CrossRef] [PubMed]
4. Bond, T.C.; Streets, D.G.; Yarber, K.F.; Nelson, S.M.; Woo, J.H.; Klimont, Z. A technology-based global inventory of black and organic carbon emissions from combustion. *J. Geophys. Res.* **2004**, *109*, D14. [CrossRef]
5. *IPCC Climate Change 2013: The Physical Science Basis, Contribution of Working Group I to the Fifth Assessment Report of the Intergovernmental Panel on Climate Change*; Cambridge University Press: Cambridge, UK; New York, NY, USA, 2013.
6. Dumka, U.C.; Kaskaoutis, D.G.; Devara, P.C.S.; Kumar, R.; Kumar, S.; Tiwari, S.; Gerasopoulos, E.; Mihalopoulos, N. Year-long variability of the fossil fuel and wood burning black carbon components at a, rural site in southern Delhi outskirts. *Atmos. Res.* **2019**, *216*, 11–25. [CrossRef]
7. Chen, W.; Tian, H.; Qin, K. Black carbon aerosol in the industrial city of Xuzhou, China: Temporal characteristics, and source appointment. *Aerosol Air Qual. Res.* **2019**, *19*, 794–811. [CrossRef]
8. AERONET. Available online: https://aeronet.gsfc.nasa.gov (accessed on 15 March 2021).
9. Che, H.; Gui, K.; Xia, X.; Wang, Y.; Holben, B.N.; Goloub, P.; Cuevas-Agulló, E.; Wang, H.; Zheng, Y.; Zhao, H.; et al. Large contribution of meteorological factors to inter-decadal changes in regional aerosol optical depth. *Atmos. Chem. Phys.* **2019**, *19*, 10497–10523. [CrossRef]
10. Chilinski, M.T.; Markowicz, K.; Zawadzk, O.; Stachlewska, I.; Lisok, J.; Makuch, P. Comparison of columnar, surface, and UAS profile of absorbing aerosol optical depth and single scattering albedo in south east Poland. *Atmosphere* **2019**, *10*, 446. [CrossRef]
11. Ran, L.; Deng, Z.Z.; Wang, P.C.; Xia, X.A. Black carbon and wavelength-dependent aerosol absorption in the North china plain based on two-year aethalometer measurement. *Atmos. Environ.* **2016**, *142*, 132–144. [CrossRef]

12. Koven, C.D.; Fung, I. Inferring dust composition from wavelength-dependent absorption in Aerosol Robotic Network (AERONET) data. *J. Geophys. Res.* **2006**, *111*, D14. [CrossRef]
13. Shin, S.-K.; Tesche, M.; Müller, D.; Noh, Y. Technical note: Absorption aerosol optical depth components from AERONET observations of mixed dust plumes. *Atmos. Meas. Tech.* **2019**, *12*, 607–618. [CrossRef]
14. Sun, E.; Xu, X.; Che, H.; Tang, Z.; Gui, K.; An, L.; Lu, C.; Shi, G. Variation in MERRA-2 aerosol optical depth and absorption aerosol optical depth over China from 1980 to 2017. *J. Atmos. Sol. Terr. Phys.* **2019**, *186*, 8–19. [CrossRef]
15. Dubovik, O.; King, M.D. A flexible inversion algorithm for retrieval of aerosol optical properties from sun and sky radiance measurements. *Geophys. Res.* **2000**, *105*, 20673–20696. [CrossRef]
16. Chew, B.N.; Campbell, J.R.; Reid, J.S.; Giles, D.M.; Welton, E.J.; Salinas, S.V.; Liew, S.C. Tropical cirrus cloud contamination in sun photometer data. *Atmos. Environ.* **2011**, *45*, 6724–6731. [CrossRef]
17. Wu, Y.; Cheng, T.; Zheng, L. Light absorption of black carbon aerosols strongly influenced by particle morphology distribution. *Environ. Res. Lett.* **2020**, *15*, 094051. [CrossRef]
18. Chin, M.; Diehl, T.; Dubovik, O.; Eck, T.F.; Holben, B.N.; Sinyuk, A.; Streets, D.G. Light absorption by pollution, dust, and biomass burning aerosols: A global model study and evaluation with AERONET measurements. *Ann. Geophys.* **2009**, *27*, 3439–3464. [CrossRef]
19. Shimizu, A.; Sugimoto, N.; Matsui, I.; Arao, K.; Uno, I.; Murayama, T.; Kagawa, N.; Aoki, K.; Uchiyama, A.; Yamazaki, A. Continuous observations of Asian dust and other aerosols by polarization lidars in China and Japan during ACE-Asia. *Geophys. Res. Atmos.* **2004**, *109*, D19S17. [CrossRef]
20. Tesche, M.; Muller, D.; Gross, S.; Ansmann, A.; Althausen, D.; Freudenthaler, V.; Weinzirl, B.; Veira, A.; Petzold, A. Optical and microphysical properties of smoke over Cape Verde inferred from multi-wavelength lidar measurements. *Tellus B Chem. Phys. Meteorol.* **2011**, *63B*, 677–694. [CrossRef]
21. Noh, Y.; Müller, D.; Lee, K.; Kim, K.; Shimizu, A.; Sano, I.; Park, C.B. Depolarization ratios retrieved by AERONET sun—Sky radiometer data and comparison to depolarization ratios measured with lidar. *Atmos. Chem. Phys.* **2017**, *17*, 6271–6290. [CrossRef]
22. Murayama, T.; Okamoto, H.; Kaneyasu, N.; Kamataki, H.; Miura, K. Application of lidar depolarization measurement in the atmospheric boundary layer: Effects of dust and sea-salt particles. *J. Geophys. Res. Atmos.* **1999**, *104*, 31781–31792. [CrossRef]
23. Cairo, F.; Di Donfrancesco, G.; Adriani, A.; Pulvirenti, L.; Fierli, F. Comparison of various linear depolarization parameters measured by lidar. *Appl. Opt.* **1999**, *38*, 4425–4432. [CrossRef] [PubMed]
24. Shin, S.K.; Tesche, M.; Kim, K.; Kezoudi, M.; Tatarov, B.; Muller, D.; Noh, Y. On the spectral depolarization and lidar ratio of mineral dust provided in the AERONET version 3 inversion product. *Atmos. Chem. Phys.* **2018**, *18*, 12735–12746. [CrossRef]
25. Tesche, M.; Ansmann, A.; Muller, D.; Althausen, D.; Mattis, I.; Heese, B.; Freudenthaler, V.; Wiegner, M.; Esselborn, M.; Pisani, G.; et al. Vertical profiling of Saharan dust with Raman LIDAR's and airborne HSRL in southern Morocco during SAMUM. *Tellus B* **2009**, *61*, 144–164. [CrossRef]
26. Li, J.; Carlson, B.E.; Lacis, A.A. Using single scattering albedo spectral curvature to characterize East Asian aerosol mixtures. *J. Geophys. Res. Atmos.* **2015**, *120*, 2037–2052. [CrossRef]
27. Bond, T.C.; Bergstrom, W. Light absorption carbonaceous particles: An investigative review. *Aerosol Sci. Technol.* **2007**, *40*, 27–67. [CrossRef]
28. Bahadur, R.; Puppala, S.P.; Xu, Y.; Ramanathan, V. Solar absorption by elemental and brown carbon determined from spectral observations. *Proc. Natl. Acad. Sci. USA* **2012**, *109*, 17366–17371. [CrossRef]
29. Yue, S.; Hashino, M. Temperature trends in Japan: 1900–1996. *Theor. Appl. Climatol.* **2003**, *75*, 15–27. [CrossRef]
30. Ahmad, I.; Tang, D.; Wang, T.F.; Wang, M.; Wagan, B. Precipitation trend over time using Mann-Kendall and Spearman's rho tests in Swat river basin, Pakistan. *Adv. Meteorol.* **2015**, *2015*, 431860. [CrossRef]
31. Srivastava, A.; Saran, S. Comprehensive study on AOD trends over the Indian subcontinent: A statistical approach. *Int. J. Remote Sens.* **2017**, *38*, 5127–5149. [CrossRef]
32. Coen, M.C.; Andrews, E.; Asmi, A.; Baltensperger, U.; Bukowiecki, N.; Day, D.; Fiebig, M.; Fjaeraa, A.M.; Flentje, H.; Hyvärinen, A.; et al. Aerosol decadal trends—Part 1: In-situ optical measurements at GAW and IMPROVE stations. *Atmos. Chem. Phys.* **2013**, *13*, 869–894. [CrossRef]
33. Mann, H.B. Nonparametric test against trend. *Econometrica* **1945**, *13*, 245–259. [CrossRef]
34. Kendall, M.G. Kendall Rank Correlation Coefficient. In *The Concise Encyclopedia of Statistics*, 2008 ed.; Springer: New York, NY, USA, 2008. [CrossRef]
35. Yadav, R.; Tripathi, S.K.; Pranuthi, G.; Dubey, S.K. Trend analysis by Mann-Kendall test for precipitation and temperature for thirteen districts of Uttarakhand. *J. Agrometeorol.* **2014**, *16*, 164–171.
36. Sen, P.K. Estimates of the regression coefficient based on Kendall's tau. *J. Am. Stat. Assoc.* **2012**, *63*, 1379–1389. [CrossRef]
37. Qin, W.; Liu, Y.; Wang, L.; Lin, A.; Xia, X.; Che, H.; Bilal, M.; Zhang, M. Characteristic and driving factors of aerosol optical depth over mainland China during 1980–2017. *Remote Sens.* **2018**, *10*, 1064. [CrossRef]
38. Maghrabi, A.H.; Alotaibi, R.N. Long term variations of AOD from an AERONET station in the central Arabian Peninsula. *Theor. Appl. Climatol.* **2017**, *134*, 1015–1026. [CrossRef]
39. Cheng, N.; Cheng, B.; Li, S.; Ning, T. Effects of meteorology and emission reduction measures on air pollution in Beijing during heating seasons. *Atmos. Pollut. Res.* **2019**, *10*, 971–979. [CrossRef]
40. Hazra, A. Using the confidence interval confidently. *J. Thorac. Dis.* **2017**, *9*, 4125–4130. [CrossRef]

41. Li, J.; Carlson, B.E.; Dubovik, O.; Lacis, A.A. Recent trends in aerosol optical properties derived from AERONET measurements. *Atmos. Chem. Phys.* **2014**, *14*, 12271–12289. [CrossRef]
42. Pozzer, A.; de Meij, A.; Yoon, J.; Tost, H.; Georgoulias, A.K.; Astitha, M. AOD trends during 2001–2010 from observations and model simulations. *Atmos. Chem. Phys.* **2015**, *15*, 5521–5535. [CrossRef]
43. Soni, M.; Chandel, A.S.; Verma, S.; Payra, S.; Prakash, D.; Holben, B. Aerosols properties over desret influenced locations situated in four different continents. *Atmos. Environ.* **2021**, *248*, 118232. [CrossRef]
44. Prospero, J.M.; Ginoux, P.; Torres, O.; Nicholson, S.E.; Gill, T.E. Environmental characterization of global sources of atmospheric soil dust identified with the Nimbus 7 Total Ozone Mapping Spectrometer (TOMS) absorbing aerosol product. *Rev. Geophys.* **2002**, *40*, 1. [CrossRef]
45. Horowitz, H.M.; Garland, R.M.; Thatcher, M.; Landman, W.A.; Dedekind, Z.; Merwe, J.; Engelbrecht, F.A. Evaluation of climate model aerosol seasonal and spatial variability over Africa using AERONET. *Atmos. Chem. Phys.* **2017**, *17*, 13999–14023. [CrossRef]
46. Lieke, K.; Kandler, K.; Scheuvens, D.; Emmel, C.; Von Glahn, C.; Petzold, A.; Weinzierl, B.; Veira, A.; Ebert, M.; Weinbruch, S.; et al. Particle chemical properties in the vertical column based on aircraft observations in the vicinity of Cape Verde Islands. *Tellus B* **2011**, *63*, 497e511. [CrossRef]
47. Omari, K.; Abuelgasim, A.; Alhebsi, K. Aerosol optical depth retrieval over the city of Abu Dhabi, United Arab Emirates (UAE) using Landsat-8 OLI images. *Atmos. Pollut. Res.* **2019**, *10*, 1075–1083. [CrossRef]
48. Alpert, P.; Shvainshtein, O.; Kishcha, P. AOD Trends over Megacities based on Space Monitoring Using MODIS and MISR. *Am. J. Clim. Chang.* **2012**, *1*, 117–131. [CrossRef]
49. Carabali, G.; Estevez, H.R.; Valdes-Barron, M.; Bonifaz-Alfonzo, R.; Riveros-Rosas, D.; Velasco-Herrera, V.M.; Vazquez-Galvez, F. Aerosol climatology over the Mexico City basin: Characterization of optical properties. *Atmos. Res.* **2017**, *194*, 190–201. [CrossRef]
50. Zhang, Y.; Yu, H.; Eck, T.E.; Smirnov, A.; Chin, M.; Remer, L.A.; Bian, H.; Tan, Q.; Levy, R.; Holben, B.N.; et al. Aerosol daytime variations over North and South America derived from multiyear AERONET measurements. *J. Geophys. Res. Atmos.* **2012**, *117*, D5. [CrossRef]
51. Just, A.C.; Wright, R.O.; Schwartz, J.; Coull, B.A.; Baccarelli, A.A.; Tellez-Rojo, M.M.; Moody, E.; Wang, Y.; Lyapustin, A.; Kloog, A. Using High-Resolution Satellite Aerosol Optical Depth to Estimate Daily $PM_{2.5}$ Geographical Distribution in Mexico City. *Environ. Sci. Technol.* **2015**, *49*, 8576–8584. [CrossRef]
52. Saldiva, P.H.; Pope, C.A., III; Schwartz, J.; Dockery, D.W.; Lichtenfels, A.J.; Salge, J.M.; Barone, I.; Bohm, G.M. Air Pollution and Mortality in Elderly People: A Time-Series Study in Sao Paulo, Brazil. *Arch. Environ. Health Int. J.* **1995**, *50*, 159–163. [CrossRef]
53. Meij, A.D.; Pozzer, A.; Lelieveld, J. Trend analysis in aerosol optical depths and pollutant emission estimates between 2000 and 2009. *Atmos. Environ.* **2012**, *51*, 75–85. [CrossRef]
54. Dey, S.; Di Girolamo, L. A decade of change in aerosol properties over the Indian subcontinent. *Geophys. Res. Lett.* **2011**, *38*, 14. [CrossRef]
55. Central Pollution Control Board. *National Ambient Air Quality Status and Trends*; Ministry of Environment, Forest and Climate Change Government of India: New Delhi, India, 2014.
56. Singh, R.P.; Dey, S.; Tripathi, S.N.; Tare, V.; Holben, B. Variability of aerosol parameters over Kanpur, northern India. *J. Geophys. Res. Atmos.* **2004**, *109*, D23. [CrossRef]
57. Dey, S.; Tripathi, S.N.; Singh, R.P.; Holben, B.N. Sesonal variability of aerosol parameters over Kanpur, an urban site in Indo—Gangetic basin. *Adv. Space Res.* **2005**, *36*, 778–782. [CrossRef]
58. Chen, B.; Du, K.; Wang, Y.; Chen, J.; Zhao, J.; Wang, K.; Zhang, F.; Xu, L. Emission and Transport of Carbonaceous Aerosols in Urbanized Coastal Areas in China. *Aerosol Air Qual. Res.* **2012**, *12*, 371–378. [CrossRef]
59. Gu, X.; Bo, F.; Cheng, T.; Chen, H.; Wang, Y.; Guo, H. The impacts of regional transport and meteorological factors on aerosol optical depth over Beijing, 1980–2014. *Nat. Sci. Rep.* **2018**, *8*, 5113. [CrossRef] [PubMed]
60. Qu, W.; Arimoto, R.; Zhang, X.Y.; Zhao, C.H.; Wang, Y.Q.; Sheng, L.F.; Fu, G. Spatial distribution and inter annual variation of surface PM_{10} concentrations over eighty-six Chinese cities. *Atmos. Chem. Phys.* **2010**, *10*, 5641–5662. [CrossRef]
61. Wang, L.; Zhang, F.; Pilot, E.; Yu, J.; Nie, C.; Holdaway, J.; Yang, L.; Li, Y.; Wang, W.; Vardoulakis, S.; et al. Taking action on air pollution control in the Beijing-Tianjin-Hebi (BTH) region: Progress, challenges and opportunities. *Int. J. Environ. Res. Public Health* **2018**, *15*, 306. [CrossRef]
62. Ni, M.; Huang, J.; Lu, S.; Li, X.; Yan, J.; Cen, K. A review on black carbon emissions, worldwide and in China. *Chemosphere* **2014**, *107*, 83–93. [CrossRef]
63. Kanaya, Y.; Yamaji, K.; Miyakawa, T.; Taketani, F.; Zhu, C.; Choi, Y.; Komazaki, Y.; Ikeda, K.; Kondo, Y.; Klimont, Z. Rapid reduction in black carbon emissions from China: Evidence from 2009–2019 observations on Fukue Island, Japan. *Atmos. Chem. Phys.* **2020**, *20*, 6339–6356. [CrossRef]
64. Qin, W.; Zhang, Y.; Chen, J.; Yu, Q.; Cheng, S.; Li, W.; Liu, X.; Tian, H. Variation, sources and historical trend of black carbon in Beijing, China based on ground observation and MERRA-2 reanalysis data. *Environ. Pollut.* **2019**, *245*, 853–863. [CrossRef]
65. Cho, C.; Kim, S.W.; Lee, M.; Lim, S.; Fang, W.; Gustafsson, O.; Andersson, A.; Park, R.J.; Sheridan, P.J. Observation-based estimates of the mass absorption cross-section of black and brown carbon and their contribution to aerosol light absorption in East Asia. *Atmos. Environ.* **2019**, *212*, 65–74. [CrossRef]
66. Chan, K.L. Aerosol optical depths and their contributing sources in Taiwan. *Atmos. Environ.* **2017**, *148*, 364–375. [CrossRef]

67. Peralta, O.; Ortinez-Alvarez, A.; Basaldud, R. Atmospheric black carbon concentrations in Mexico. *Atmos. Res.* **2019**, *230*, 104626. [CrossRef]
68. Paredes-Miranda, G.; Arnott, W.P.; Moosmuller, H.; Green, M.C.; Gayawali, M. Black carbon aerosol concentration in five cities and its scaling with city population. *Bull. Am. Meteorol. Soc.* **2013**, *94*, 41–50. [CrossRef]
69. Ribeiro, H.; de Assuncao, J.V. Transport air pollution in Sao-Paulo, Brazil: Advances in control programs in the last 15 years. In *Transactions on State of the Art in Science and Engineering*; WIT Press: London, UK, 2005; Volume 22, ISSN 1755-8336. [CrossRef]
70. Fawole, O.G.; Cai, X.; Levine, J.G.; Pinker, R.T.; MacKenzie, A.R. Detection of a gas flaring signature in the AERONET optical properties of aerosols at a tropical station in West Africa. *J. Geophys. Res. Atmos.* **2016**, *121*, 14–513. [CrossRef]
71. Ramachandran, S.; Rajesh, T.A. Black Carbon aerosol mass concentrations over Ahmadabad, an urban location in western India: Comparison with urban sites in Asia, Europe, Canada, and the United States. *J. Geophys. Res. Atmos.* **2007**, *112*, D6. [CrossRef]
72. Kutzner, D.D.; von Schneidemesser, E.; Kuik, F.; Quedenau, J.; Waetherhead, E.C.; Schmale, J. Long-Term monitoring of black carbon across Germany. *Atmos. Environ.* **2018**, *185*, 41–52. [CrossRef]
73. Romppanen, S. Arctic governance via EU law on black carbon? *Rev. Eur. Comp. Int. Environ. Law* **2018**, *27*, 45–54. [CrossRef]
74. Thomas, L.B. Black Carbon Problems in Transportation: Technological Solutions and Governmental Policy Solutions. In *Massachusetts Institute of Technology Working Paper Series 1–25*; CEEPR, MIT Center for Energy and Environmental Policy Research: Cambridge, MA, USA, 2017. Available online: https://ceepr.mit.edu/wp-content/uploads/2021/09/2017-012.pdf (accessed on 25 June 2021).
75. SAFAR (System for Air Quality Forecasting and Research). *A Special Report Emission Inventory for National Capital Region Delhi Ministry of Earth Sciences*; Government of India: Pune, India, 2010. Available online: http://safar.tropmet.res.in (accessed on 10 July 2021).
76. Venkataraman, C.; Habib, G.; Eiguren-Fernandez, A.; Miguel, A.H.; Friedlander, S.K. Residential biofuels in South Asia: Carbonaceous aerosol emissions and climate impacts. *Science* **2005**, *307*, 1454–1456. [CrossRef] [PubMed]
77. David, L.M.; Ravishankara, A.R.; Kodros, J.K.; Venkataraman, C.; Sadavarte, P.; Pierce, J.R.; Chaliyakunnel, S.; Millet, D.B. Aerosol Optical Depth Over India. *J. Geophys. Res. Atmos.* **2018**, *123*, 3688–3703. [CrossRef]
78. Ali, M.A.; Nichol, J.E.; Bilal, M.; Qiu, Z.; Mazhar, U.; Wahiduzzaman, M.; Almazroui, M.; Islam, M.N. Classification of aerosols over Saudi Arabia from 2004–2016. *Atmos. Environ.* **2020**, *241*, 117785. [CrossRef]
79. Cao, J.J.; Zhu, C.S.; Chow, J.C.; Watson, J.G.; Han, Y.M.; Wang, G.H.; Shen, Z.X.; An, Z.S. Black carbon relationships with emissions and meteorology in Xi'an, China. *Atmos. Res.* **2009**, *94*, 194–202. [CrossRef]
80. Liu, Y.; Yan, C.; Zheng, M. Source apportionment of black carbon during winter in Beijing. *Sci. Total Environ.* **2017**, *618*, 531–541. [CrossRef] [PubMed]
81. Dehkhoda, N.; Noh, Y.; Joo, S. Long-Term Variation of Black Carbon Absorption Aerosol Optical Depth from AERONET Data over East Asia. *Remote Sens.* **2020**, *12*, 3551. [CrossRef]
82. Kang, L.; Chen, S.; Huang, J.; Zhao, S.; Ma, X.; Yuan, T.; Zhang, X.; Xie, T. The spatial and temporal distributions of absorbing aerosols over East Asia. *Remote Sens.* **2017**, *9*, 1050. [CrossRef]
83. Castanho, A.; Artaxo, P. Wintertime and summertime Sao Paulo aerosol source apportionment study. *Atmos. Environ.* **2001**, *35*, 4889–4902. [CrossRef]
84. Chiloane, K.E.; Beukes, J.P.; van Zyl, P.G.; Maritz, P.; Vakkari, V.; Josipovic, M.; Venter, A.D.; Jaars, K.; Tiitta, P.; Kulmala, M.; et al. Spatial, temporal and source contribution assessments of black carbon over the northern interior of South Africa. *Atmos. Chem. Phys.* **2017**, *17*, 6177–6196. [CrossRef]
85. Liakakou, E.; Stavroulas, I.; Kaskaoutis, D.G.; Grivas, G.; Paraskevopoulou, D.; Dumka, U.C.; Tsagkaraki, M.; Bougiatioti, A.; Oikonomou, K.; Sciare, J.; et al. Long-term variability, source apportionment and spectral properties of black carbon at an urban bachground site in Athens, Greece. *Atmos. Environ.* **2020**, *222*, 117137. [CrossRef]
86. Bikkina, S.; Andersson, A.; Ram, K.; Sarin, M.M.; Sheesley, R.J.; Kirillova, E.N.; Rengarajan, R.; Sudheer, A.K.; Gustafsson, Ö. Carbon isotope-constrained seasonality of carbonaceous aerosol sources from an urban location (Kanpur) in the Indo-Gangetic Plain. *J. Geophys. Res. Atmos.* **2017**, *122*, 4903–4923. [CrossRef]
87. Tiwari, S.; Srivastava, A.K.; Bisht, D.S.; Bano, T.; Singh, S.; Behura, S.; Srivastava, M.K.; Chate, D.M.; Padmanabhamurty, B. Black carbon and chemical characteristics of PM_{10} and $PM_{2.5}$ at an urban site of North India. *J. Atmos. Chem.* **2009**, *62*, 193–209. [CrossRef]
88. Ynoue, R.Y.; Andrade, M.F. Size-Resolved Mass Balance of Aerosol Particles over the Sao Paulo Metropolitan Area of Brazil. *Aerosol Sci. Technol.* **2004**, *38*, 52–62. [CrossRef]
89. Costabile, F.; Angelini, F.; Barnaba, F.; Gobbi, G.P. Partitioning of black carbon between ultrafine and fine particle modes in an urban airport vs. urban background environment. *Atmos. Environ.* **2015**, *102*, 136–144. [CrossRef]
90. Petzold, A.; Gysel, M.; Vancassel, X.; Hitzenberger, R.; Puxbaum, H.; Vrochticky, S.; Weingartner, E.; Baltensperger, U.; Mirabel, P. On the effects of organic matter and sulphur-containing compounds on the CCN activation of combustion particles. *Atmos. Chem. Phys.* **2005**, *5*, 31873203. [CrossRef]
91. Jacobson, M.Z. Short-term effects of controlling fossil-fuel soot biofuel soot and gases, and methane on climate, Arctic ice, and air pollution health. *Geophys. Res. Atmos.* **2010**, *115*, 1307–1314. [CrossRef]
92. Wu, Y.; Cheng, T.; Liu, D.; Allen, J.D.; Zheng, L.; Chen, H. Light absorption enhancement of black carbon aerosol constrained by particle morphology. *Environ. Sci. Technol.* **2018**, *52*, 6912–6919. [CrossRef]

93. Schwarz, J.P.; Gao, R.S.; Spackman, J.R.; Watts, L.A.; Thomson, D.S.; Fahey, D.W.; Ryerson, T.B.; Peischl, J.; Holloway, J.S.; Trainer, M.; et al. Measurements of the mixing state, mass, and optical size of individual black carbon particles in urban and biomass burning emissions. *Geophys. Res. Lett.* **2008**, *35*, 13. [CrossRef]
94. Mayol-Bracero, O.L.; Guyon, P.; Graham, B.; Roberts, G.; Andreae, M.O.; Decesari, S.; Facchini, M.C.; Fuzzi, S.; Artaxo, P. Water-soluble organic compounds in biomass burning aerosols over Amazonia 2. Apportionment of the chemical composition and importance of the polyacidic fraction. *J. Geophys. Res.* **2002**, *107*, 8091. [CrossRef]
95. Wang, J.; Liu, D.; Ge, X.; Wu, Y.; Shen, F.; Chen, M.; Zhao, J.; Xie, C.; Wang, Q.; Xu, W.; et al. Characterization of black carbon-containing fine particles in Beijing during wintertime. *Atmos. Chem. Phys.* **2019**, *19*, 447–458. [CrossRef]
96. Zhao, D.; Liu, D.; Yu, C.; Tian, P.; Hu, D.; Zhou, W.; Ding, S.; Hu, K.; Sun, Z.; Huang, M.; et al. Vertical evolution of black carbon characteristics and heating rate during a haze event in Beijing winter. *Sci. Total Environ.* **2020**, *709*, 136251. [CrossRef]